

3D LiDAR Aided GNSS and Its Tightly Coupled Integration with INS Via Factor Graph Optimization

Weisong Wen

Department of Mechanical Engineering, The Hong Kong Polytechnic University, Hong Kong, China;

BIOGRAPHY

Weisong Wen was born in Ganzhou, Jiangxi, China. He is currently a Ph.D. candidate in the Department of Mechanical Engineering, The Hong Kong Polytechnic University. His research interests include GNSS positioning, 3D LiDAR SLAM, and multi-sensor integration for autonomous vehicles in urban areas. He was also a visiting student researcher at the University of California, Berkeley (UCB) in 2018.

ABSTRACT

Global navigation satellite system (GNSS) positioning is an indispensable source of data for providing absolute positioning for autonomous driving vehicles (ADV). Satisfactory accuracy can be obtained in sparse areas. However, the performance of GNSS can be significantly degraded by signal reflections from buildings, causing multipath effects and non-line-of-sight (NLOS) receptions. State-of-the-art 3D mapping aided (3DMA) GNSS can significantly mitigate the effects of signal reflections caused by static buildings. However, this approach relies heavily on an initial guess of the GNSS receiver, and on the availability of 3D building models. Moreover, the NLOS reception caused by surrounding dynamic objects, such as double-decker buses, cannot be mitigated. To fill this gap, in this paper we propose a novel 3D LiDAR aided GNSS positioning method which makes use of an onboard 3D LiDAR sensor to detect and correct NLOS reception caused by both static buildings and dynamic objects. A novel sliding window map surrounding the ego-vehicle is first generated, based on real-time 3D point clouds from a 3D LiDAR sensor. Then, NLOS receptions are detected based on a real-time sliding window map using a proposed fast searching method. The proposed NLOS detection method does not rely on the initial guess of the GNSS receiver. Instead of directly excluding the detected NLOS satellites from further positioning estimation, the algorithm reported in this paper rectifies the pseudorange measurement model by (1) correcting the pseudorange measurements if the reflecting point of NLOS signals is detected inside the sliding window map, and (2) remodeling the uncertainty of the NLOS pseudorange measurement using a new weighting scheme. Finally, both the corrected and healthy pseudorange measurements are tightly integrated with an inertial navigation system (INS) using factor graph optimization (FGO). We evaluated the performance of the proposed method in two typical urban canyons in Hong Kong and found that improved accuracy is obtained even in such environments.

1. INTRODUCTION

Positioning in urban environments is becoming essential due to the increasing demand for autonomous driving vehicles (ADV) [1]. To achieve Level 4 [2] autonomous driving capability in all scenarios, centimeter-level absolute positioning is required. The global navigation satellite system (GNSS) [3] is currently one of the principal means of providing globally-referenced positioning for autonomous driving vehicle localization. With the increased availability of multiple satellite constellations, GNSS can provide satisfactory performance in open-sky areas, with a positioning error of around five meters [4]. However, positioning error can be up to 50 meters in highly-urbanized cities such as Hong Kong [4], due to signal reflection caused by static buildings and dynamic objects [5] such as double-decker buses. If the direct light-of-sight (LOS) is blocked, and reflected signals from the same satellite are received, the notorious non-light-of-sight (NLOS) receptions occur. According to a recent review paper [6], NLOS is currently the major difficulty in the use of GNSS in intelligent transportation systems. Because of NLOS receptions, the performance of GNSS positioning is highly influenced by real-time surrounding environmental features, such as buildings and dynamic objects. Effectively sensing and understanding surrounding environments is the key to improving GNSS positioning in urban areas, as GNSS positioning relies heavily on sky view visibility. Research into mitigating the effects of NLOS receptions in urban canyons can be divided into four areas: (1) 3D mapping-aided GNSS; (2) robust model-aided GNSS positioning; (3) camera-aided GNSS positioning; and (4) 3D LiDAR-aided GNSS positioning.

3D mapping-aided (3DMA) GNSS: Utilizing 3D building models to detect NLOS is straightforward. NLOS satellites can be detected with the aid of 3D models of buildings, and can then be excluded from use in GNSS positioning [7, 8]. However, NLOS exclusion will distort the perceived geometric distribution of the satellites, degrading accuracy [9], and even resulting in too few satellites for further GNSS calculation [9]. Moreover, these methods require the availability of 3D building models of the environment, and the performance of NLOS detection relies on the accuracy of an initial guess of the GNSS receiver's position. In addition, NLOS reception caused by dynamic objects cannot be detected as well. A well-known method, GNSS shadow matching, was developed to match measured satellite visibility with the predicted satellite visibility of hypothesized positions [10-12]. However, the performance of shadow matching is dependent upon the quality of satellite visibility classification and the initial guess as to the position of the GNSS receiver. A likelihood-based 3DMA GNSS method, which modeled the measurement uncertainty, and used this value to mitigate NLOS effects, has been proposed to provide accurate positioning in the along-street direction [13]. Due to the complementarity of the shadow matching and likelihood-based 3DMA GNSS, approaches to the integration of these approaches have recently been studied [14]. Another range-based 3DMA GNSS method is to correct the NLOS affected measurements for GNSS positioning [15-18]. These methods were proposed to simulate signal transmission routes, using a ray-tracing method. However, these ray-tracing-based 3DMA GNSS methods have the drawbacks of requiring stringency in 1) the accuracy of 3D mapping databases; 2) the initial guess of receiver positions; and 3) the computational power of the processors due to the ray-tracing process. Recently, a skymask-based NLOS correction method has been proposed [19], which effectively reduces the computational load incurred by ray-tracing-based methods [15-18]. However, these 3D mapping-aided GNSS have the drawbacks of: 1) reliance on the availability of 3D building models; 2) inability to mitigate NLOS receptions caused by surrounding dynamic objects.

Robust model-aided GNSS positioning: Instead of using additional information from 3D building models, a team from the Chemnitz University of Technology employed a robust model [20-22] to mitigate the effects of NLOS signals in GNSS single point positioning (SPP). In their earliest work, as reported in [23], a state-of-the-art factor graph [24], which makes use of all of the available historical GNSS measurements to estimate the state set of the GNSS receiver, was applied to GNSS positioning. The improved performance was obtained compared with the conventional weighted least squares (WLS) approach. This improvement was primarily because the factor graph also explores the correlation between consecutive epochs of GNSS measurements. Interestingly, the work described in [25] included a switchable constraint in the factor graph to model the probability of one satellite being an unhealthy measurement, either multipath or NLOS receptions. According to [25], the switchable constraint can effectively mitigate the effects caused by NLOS and multipath, so-called outliers in [25]. However, a major drawback is that the switchable constraint relies heavily on the initial guess of the prior factor [25], which requires a large number of hyperparameters, making it difficult to tune. Inspired by a covariance estimation technique used in the field of robotics [26], dynamic covariance estimation (DCE) [22] has been studied as a means by which to adaptively model the uncertainty of GNSS measurements. In this research, the covariance of GNSS measurements is treated as an unknown variable to be estimated in the factor graph optimization (FGO). In other words, the position of the GNSS receiver and the uncertainty in the measurement of GNSS are estimated simultaneously. Finally, the NLOS satellites are de-weighted from the FGO. Significantly improved results were obtained when the number of healthy measurements was more than the number of unhealthy measurements, such as NLOS receptions. However, it is difficult to satisfy this assumption in dense urban areas, and the DCE requires numerous parameterization as well. To get rid of the excessive parameterization, a Gaussian mixture model (GMM) [20, 21] has been proposed for modelling the uncertainty of GNSS pseudorange measurements. According to the evaluation reported in [21], the noise model of GNSS measurements is not subject to the Gaussian assumption due to the long tail of the distribution, which is caused by NLOS receptions [21]. Therefore, a GMM was employed to model the noise of the GNSS measurements, and an expectation-maximization (EM) algorithm was applied to estimate the parameters of the GNSS noise model. Then, the GMM was applied to the FGO. This is the first work to date to make use of GMM to model the uncertainty of GNSS measurements in factor graph optimization. Better and more robust performance can be obtained using this approach than can be achieved by methods using Gaussian noise, switchable constraints, or DCE. However, a major drawback of the GMM-based method is that the estimation of the parameter values of the GMM relies heavily on the accuracy of the initial guess of the position of the GNSS receiver, which is in fact similar to range-based 3DMA GNSS [15-18]. The sensitivity of the parameter estimation of GMM with respect to the initial position guess is still an open question. A team from West Virginia University (WVU) carried out similar research [27-29], applying robust models to GNSS precise point positioning (PPP) and obtained improved results.

Camera-aided GNSS positioning: Another research approach makes use of a camera to capture the environment surrounding the GNSS receiver. This approach is called camera-aided GNSS positioning [30, 31]. The camera was used to capture a sky view and establish satellite visibility. To detect the visibility of satellites, the researchers applied omnidirectional or fisheye cameras [30, 32, 33]. NLOS receptions could be detected in conjunction with the captured sky views, and improvements obtained after excluding all of the NLOS receptions detected from GNSS positioning. A major advantage of this approach is that camera-based NLOS detection relaxes the requirement of the initial guess of the position of the GNSS receiver, compared with the 3D building models-based method [7, 8]. NLOS receptions caused by dynamic objects can also be detected. Similar research [34, 35] has been conducted recently, in which improved GNSS positioning was integrated with visual simultaneous localization and mapping

(VSLAM) [36]. Unfortunately, these methods still tend to exclude NLOS receptions from GNSS positioning, and so are not applicable in dense urban areas, such as Hong Kong, Tokyo, and New York. Instead of excluding all NLOS satellites from the GNSS positioning, our recent research, as reported in [37], showed the feasibility of remodeling the NLOS satellites after detecting NLOS receptions using a fisheye camera. However, the camera is sensitive to the conditions of illumination. Moreover, the classification of satellite visibility relies heavily on the quality of the sky view, and on non-sky view area segmentation [37]. The installation of sky-pointing cameras for autonomous driving vehicles is not always possible.

3D LiDAR aided (3DLA) GNSS positioning: Recently, 3D LiDAR sensors, the so-called “eyes” of ADV, the typical indispensable onboard sensor for autonomous driving vehicles, have been used to detect NLOS caused by dynamic objects [5]. The typical dynamic object, the Hong Kong double-decker bus, was detected based on real-time 3D point clouds to identify NLOS signals blocked by the bus, but reflected by surrounding buildings. A static experiment was first performed to demonstrate the phenomenon of NLOS receptions caused by a double-decker bus. The dynamic experiment was conducted to investigate performance improvements produced by detecting and excluding NLOS receptions caused by dynamic objects from use in further GNSS positioning. According to the experiments, more than five meters of positioning error can be introduced by the detected NLOS. In short, the NLOS receptions can be caused by dynamic objects which should also be solved. However, the method proposed in [5] relies heavily on the accuracy of object detection. Due to the limited field of view (FOV: $-30^{\circ} \sim +10^{\circ}$) of 3D LiDAR, only part of a double-decker bus can be scanned. However, to the best of our knowledge, this is the first work that employed object detection to help GNSS positioning. Instead of detecting only dynamic objects, we also explored the detection of surrounding static buildings using 3D LiDAR point clouds [9]. Due to the limited field of view of 3D LiDAR, only part of the buildings can be scanned. Therefore, information about building height is required [9]. Given this information, NLOS receptions caused by the buildings can be detected. Instead of excluding the detected NLOS receptions, we explored ways in which to correct NLOS pseudorange measurements with the help of LiDAR, which can measure the distance from the GNSS receiver to the surface of a building which may have reflected the GNSS signal. Then the corrected and the healthy GNSS measurements can both be used in further GNSS positioning. The improved performance was obtained after correcting the detected NLOS satellites. Unlike 3DMA GNSS, the method proposed in [9] reduces the importance of the initial guess of the position of the GNSS receiver. Unfortunately, the performance of this approach [9] relies on the accuracy of the detection of buildings and reflectors. Both building detection and reflector detection can fail when a building surface is irregular. The limited FOV of LiDAR remains a drawback in the detection of both dynamic objects and buildings. Overall, the work reported in [5] and [9] shows the feasibility of detecting GNSS NLOS using real-time onboard sensing: the real-time point clouds. To overcome the drawback of the limited FOV of 3D LiDAR, we explored the use of both fish-eye cameras and 3D LiDAR to detect and correct NLOS signals [38]. The fish-eye camera was applied to detect NLOS signals and the 3D LiDAR was employed to measure the distance between the GNSS receiver and a potential reflector causing NLOS signals. However, this approach shares the problems with the work described in [30, 31].

In short, state-of-the-art 3DMA GNSS relies on an initial guess of the position of the GNSS receiver, and on the availability of 3D building models. The GMM-based method obtains the best performance of all the robust model-based solutions discussed. However, it relies heavily on an initial guess of the position of the receiver. The camera aided GNSS positioning has effectively relaxed the requirement for the initial guess. However, problems caused by the sensitivity of the camera to the illumination level are still an unsolved problem. 3D LiDAR aided GNSS positioning is an innovative solution for mitigating the effects of NLOS receptions and has several advantages: (1) both dynamic and static objects can be considered during NLOS detection; (2) NLOS detection does not rely on an initial guess of the position of the GNSS receiver; (3) the approach does not require the use of 3D building models, and 3D LiDAR is robust against illumination conditions. However, there are still three major drawbacks: (1) the limited FOV of 3D LiDAR causes limited environment sensing capability; (2) the performance of NLOS detection relies heavily on the accuracy of object detection, such as double-decker bus detection in [5] and building detection in [9]; and (3) the reflector detection method described in [5] [9] [38] can only work when a building surface is detected and is sufficiently regular.

In this paper, we relaxed the three above-listed drawbacks of the previous 3D LiDAR aided (3DLA) GNSS positioning. First, a novel sliding window map (SWM) was generated based on real-time 3D point clouds from 3D LiDAR. Only the 3D point clouds inside a sliding window were employed to generate the SWM, as the point clouds far away from the GNSS receiver are not needed for NLOS detection. The environment description capability of SWM is significantly better than that of 3D real-time point clouds. Therefore, the FOV of LiDAR sensing is effectively enhanced (**relax the drawback 1**). Moreover, the magnitude of the drift of the SWM is bounded to a small value. As the generated SWM is in the body frame, which is located at the center of the 3D LiDAR, the orientation is directly adopted from an attitude and heading reference system (AHRS) to transform the SWM from the body frame to a local (ENU) frame [3]. Then, NLOS receptions are directly detected based on real-time SWM, which does not require object detection, using a fast searching method (**relax the drawback 2**). More importantly, the proposed NLOS detection method does not rely on the initial guess of the GNSS receiver. Instead of directly excluding detected NLOS satellites from use in further positioning estimation, this work proposes an approach to rectify the pseudorange measurement model by (1) correcting the pseudorange measurements if the reflecting point of the NLOS signals is detected based on a

constrained searching method (**relax the drawback 3**) inside the dense SWM; and (2) re-modeling the uncertainty of NLOS pseudorange measurement using a novel weighting scheme if the reflector is not detected. Finally, both the corrected and healthy pseudorange measurements are tightly coupled with an inertial navigation system (INS) using factor graph optimization to see the potential of the proposed 3D LiDAR aided GNSS in sensor integration. The main contributions of this paper are as follows: (1) This paper is the continuous work in [5, 9, 38, 39], and the three listed drawbacks of the previous 3D LiDAR aided GNSS are relaxed in this paper. (2) This approach effectively makes use of all the historical measurements to integrate with the onboard INS, using a state-of-the-art factor graph to obtain more robust positioning performance.

The remainder of this paper is organized as follows. An overview of the proposed method is given in Section 2. The generation of the sliding window map is elaborated in Section 3. In Section 4, the proposed NLOS detection, NLOS correction, and remodeling approaches are presented. Section 5 presents GNSS/INS integration using FGO based on the rectified and the healthy GNSS measurements. Two experiments were performed to evaluate the effectiveness of the proposed method in GNSS standalone positioning and GNSS/INS integration. Finally, conclusions are drawn, and further work is presented in Section 7.

2. OVERVIEW OF THE PROPOSED METHOD

An overview of the method proposed in this paper is shown in Fig. 1. The system consists of two parts: the 3D LiDAR aided GNSS part, and the GNSS/INS integration part. The inputs of the system include (1) raw data (A_t) from the accelerometer and orientation from AHRS (R_t) at a given epoch t ; (2) 3D real-time point clouds (S_t) from a 3D LiDAR sensor; and (3) raw GNSS pseudorange measurements (SV_t^{all}) from a GNSS receiver. The output of the system is the state of the GNSS receiver. First, the 3D point clouds within a sliding window are employed to generate the SWM (M_t), which is described in Section 3. As the LiDAR point cloud is originally fixed at the body frame, the center of the 3D LiDAR, the orientation data from the AHRS are used to transform the point clouds to the local (ENU) frame [3]. NLOS detection is next performed based on the raw GNSS measurements, SV_t^{all} , and the SWM, using the fast searching method described in Section 4. The output of the NLOS detection step is an estimation of satellite visibility (Vis_t). Reflecting point detection is next conducted to find the potential point which reflects the NLOS signal. The NLOS pseudorange (SV_t^C) is corrected based on an NLOS error model. If the reflecting point is not found inside the SWM, a novel remodeling scheme is applied to de-weight the NLOS measurements (SV_t^M) in further GNSS positioning and its integration with INS. Finally, both the healthy (SV_t^H) and rectified GNSS pseudorange (SV_t^C , SV_t^M) measurements are tightly integrated with the INS using a probabilistic factor graph optimization, as described in Section 5.

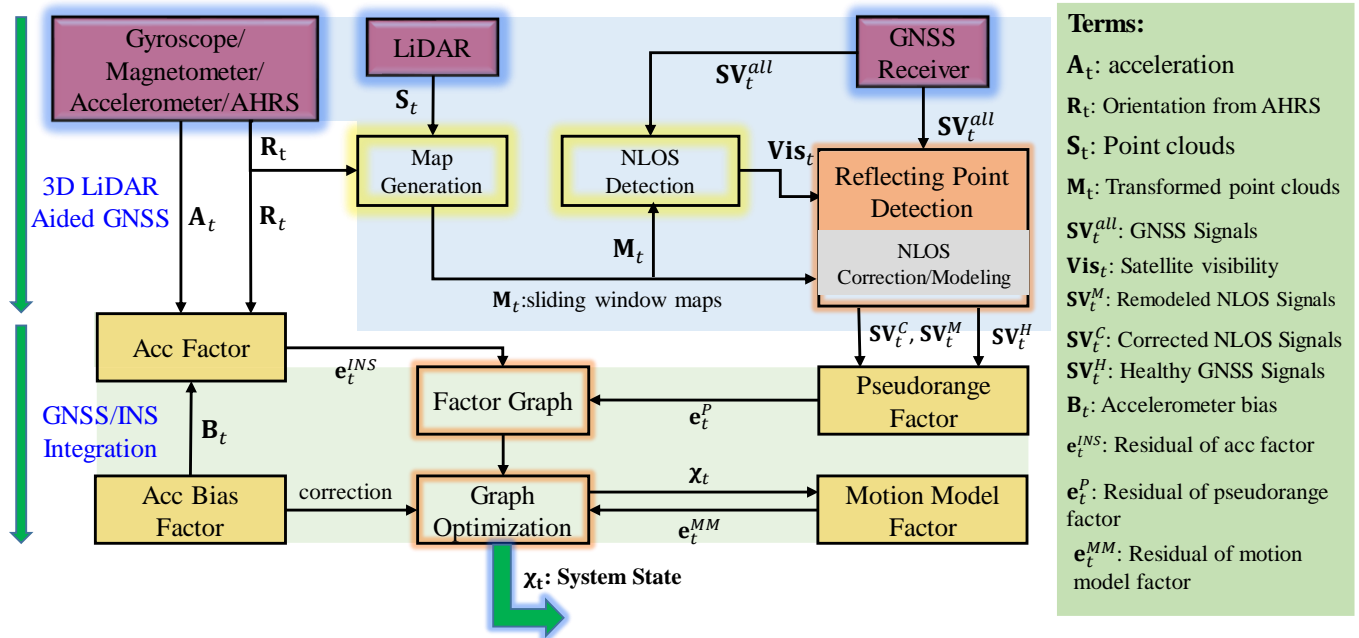


Fig. 1. Overview of the proposed method. The inputs are the raw measurements from INS, 3D LiDAR and GNSS receiver. The output is the position state of the GNSS receiver

3. SLIDING WINDOW MAP GENERATION

This section describes in detail the methodology of generating an SWM for further NLOS detection. In our previous work, described in [5, 9, 38, 39], only real-time 3D point clouds were applied in object detection to further detect the NLOS satellites caused by buildings and dynamic objects. Due to the limited FOV of 3D LiDAR, building height information is required to extend the detected building to its exact height, as described in [9]. To solve this problem, we registered real-time 3D point clouds into a map that can effectively enhance the FOV of 3D LiDAR sensing. Fig. 2 shows the difference between the real-time 3D LiDAR point clouds and the SWM. The white points in this Figure represent the real-time point clouds from the 3D LiDAR. The colored points denote the map points of the SWM. Note that the ground points were removed from the SWM for efficient NLOS detection, as described in Section 4.1.

It is clear from the Figure that only the low-lying parts of buildings or double-decker buses are scanned by the 3D LiDAR (we used Velodyne 32 [40] for the work described in this paper). The visibility of satellites with high elevation angles cannot be effectively classified simply based on real-time 3D point clouds. Real-time 3D point clouds are also sparse, due to the physical scanning angle distribution of 3D LiDAR. However, the SWM proposed in this paper can effectively ameliorate this problem. We can see from Fig. 2 that the elevation mask angle can reach 76° with the help of SWM, so the visibility of a satellite with an elevation angle of less than 76° can be classified in this case. The point clouds in SWM are significantly denser than raw real-time 3D point clouds, a factor that can contribute significantly to the accuracy of NLOS detection. A snapshot of the complete SWM map is shown at the top right of Fig. 2. Both the buildings and the dynamic objects, such as double-decker buses, and even the trees are involved in the SWM, which is not included in the 3D building model [41].

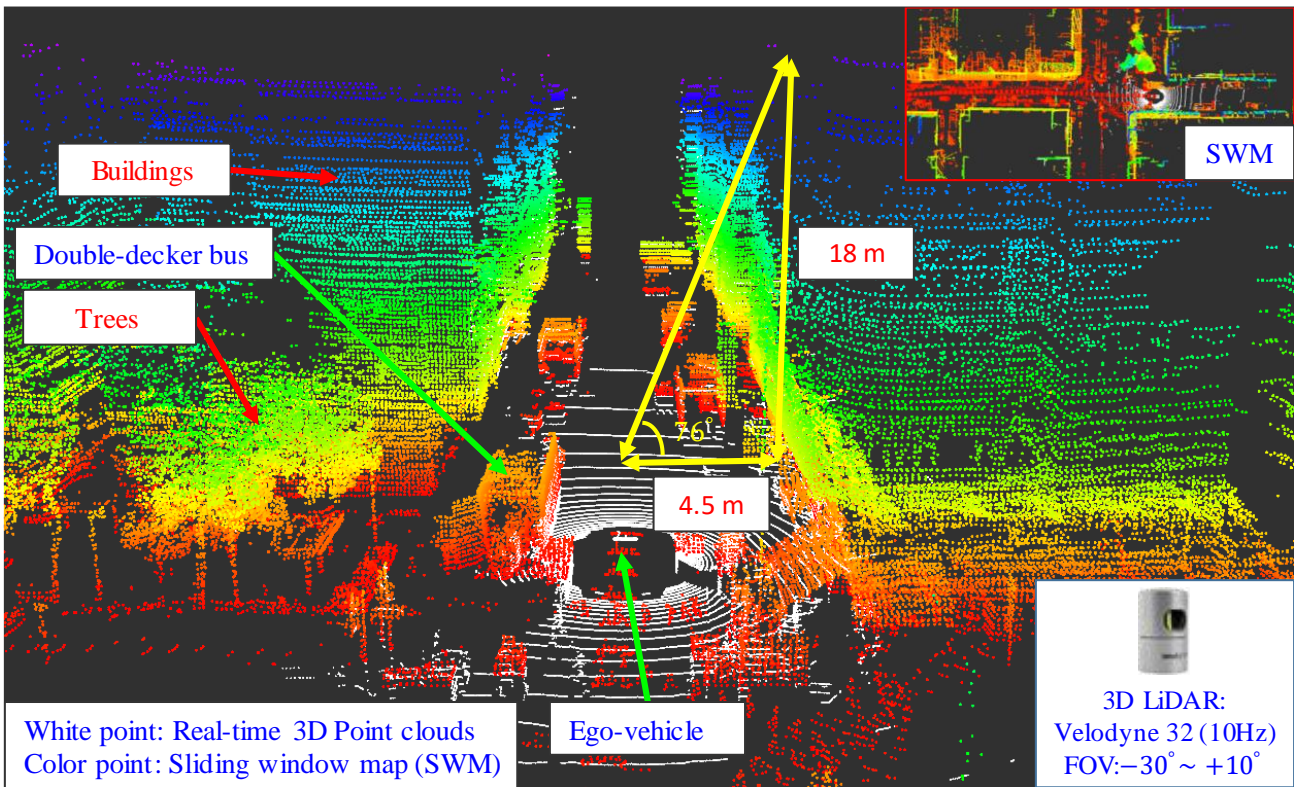


Fig. 2. Demonstration of a generated sliding window map (SWM) and the real-time 3D point clouds. The white points represent the real-time 3D point clouds. The colored points come from the SWM, and the color is determined by the height.

To generate a point cloud map based on real-time 3D point clouds, simultaneous localization, and mapping (SLAM) [42] methods have been extensively studied over the past decades. Satisfactory accuracy can be obtained in a short period with low drift [43]. However, the error can accumulate over time, causing large errors after long-term traveling. Usually, only the objects inside a circle with a radius of 250 meters can cause GNSS NLOS receptions, and buildings far away can be ignored. We, therefore, employed only the last N_{sw} frames of the 3D point clouds to generate a sliding window map. In the conventional SLAM problem [43], the map is generated by accumulating the point clouds from the first epoch, 1, to the current epoch, t , as shown in the top panel of Figure 3. The pose of the point clouds is estimated by tracking the motion between consecutive frames of point clouds. However, error accumulates from the first epoch to the current epoch. As shown in Figure 3, x_t represents the pose of the keyframe [43] at epoch t . The proposed sliding window-based map generation is shown in the bottom panel of the figure, in

which we consider only the keyframes inside a sliding window between epochs i and t . The drift error between epochs i and t for map generation is therefore bounded at a small value. The accuracy of an SWM relies heavily on the accuracy of motion estimation between consecutive frames of point clouds. In this work, we used the LiDAR odometry and mapping (LOAM) algorithm presented in [43] to generate the SWM. LOAM [43] is a state-of-the-art method that retains the top one accuracy in the KITTI dataset [44] for four years. Based on LOAM, as proposed in [43], three steps are included: feature extraction, point cloud registration, and local mapping. The rest of this section describes these three steps.

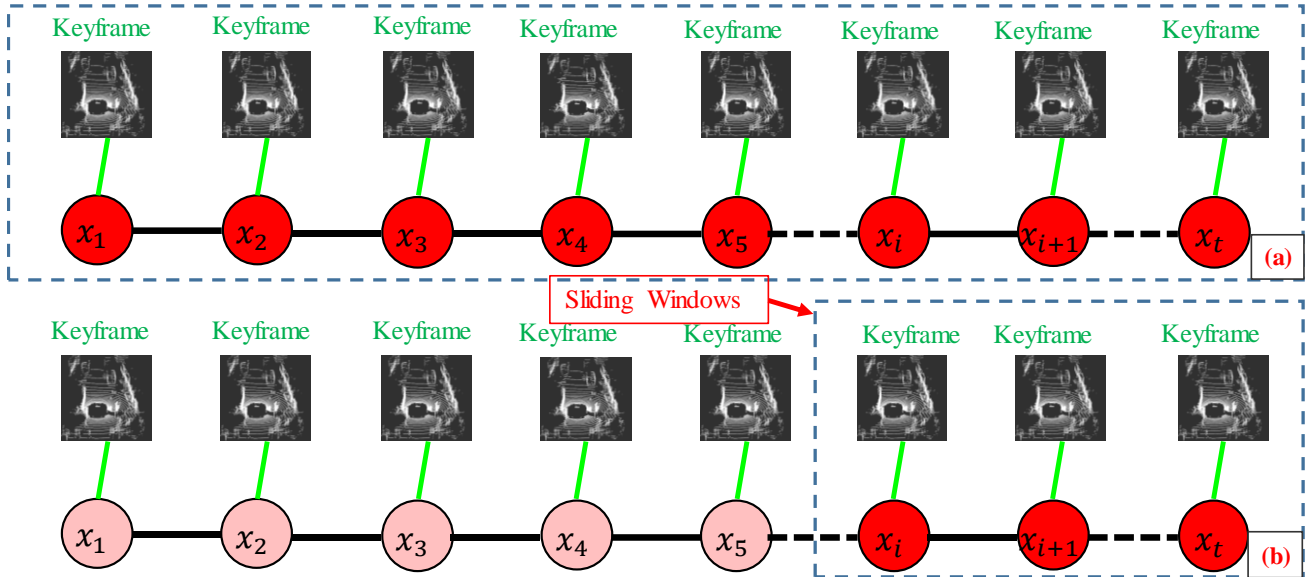


Fig. 3. Comparison of (a) the conventional full SLAM and (b) the proposed sliding window map

Feature Extraction from 3D Point Clouds: As shown in Fig. 1, the inputs into the map generation algorithm are raw 3D point clouds (\mathbf{S}_t) generated using 3DLiDAR. As described in Section 2, the orientation (\mathbf{R}_t) is used to transfer the \mathbf{S}_t to a local frame as \mathbf{P}_t . The first step is feature extraction, which is carried out based on the work reported in [43]. The input into the feature extraction algorithm is the $\mathbf{P}_t\{P_{t,1}, P_{t,2}, \dots, P_{t,i}, P_{t,N}\}$ at a frequency of 10 Hz. N denotes the number of points inside the frame of a point cloud. The points are classified as planar points or edge points, depending upon the roughness of the points. The roughness of a point is determined as follows [43]:

$$c = \frac{1}{|\mathcal{S}| \cdot \|P_{t,i}\|} \|\sum_{j \in \mathcal{S}, j \neq i} (P_{t,j} - P_{t,i})\|, \quad (1)$$

where c represents the roughness of a point, \mathcal{S} denotes a small local region near the point $P_{t,i}$, and $P_{t,j}$ indicates a point near $P_{t,i}$ inside the small local region. If the calculated roughness is larger than a pre-determined threshold [43], the point is classified as an edge point. Points with roughness lower than the threshold are classified as planar points. The output of the feature extraction process is the feature set $\mathbf{F}_t\{F_t^p, F_t^e\}$, in which F_t^p and F_t^e are feature sets containing all planar and edge points, respectively.

Point cloud registration: Point cloud registration is a process that estimates the relative motion between two consecutive frames of point clouds. The relative motion is calculated using point-to-edge and point-to-plane scan matching. The objective of this process is to find corresponding features for points in $\mathbf{F}_t\{F_t^p, F_t^e\}$ from the feature points set $\mathbf{F}_{t-1}\{F_{t-1}^p, F_{t-1}^e\}$. The detailed steps can be found in [43]. The point cloud registration process is as follows:

$$\mathbf{m}_{t-1,PR}^{t,PR} = \text{PCR}(\mathbf{F}_t\{F_t^p, F_t^e\}, \mathbf{F}_{t-1}\{F_{t-1}^p, F_{t-1}^e\}), \quad (2)$$

where PCR denotes the point cloud registration function. The output of the point cloud registration process is the approximate relative motion, $\mathbf{m}_{t-1,PR}^{t,PR}$, at a frequency of 10 Hz.

Local mapping: To refine the relative motion estimation, the local mapping process based on [43] is applied to refine the motion estimation, $\mathbf{m}_{t-1,PR}^{t,PR}$. A detailed description can be found in [43]. The principle of the mapping process is that the extracted $\mathbf{F}_t\{F_t^p, F_t^e\}$ is mapped into the incrementally-built map to refine the motion estimate, $\mathbf{m}_{t-1,PR}^{t,PR}$. The output of local mapping is refined motion estimation, $\mathbf{m}_{t-1,LM}^{t,LM}$. All motion transformations between the keyframes in epochs i to k can be estimated, and

the SWM obtained as \mathbf{M}_t . Note that \mathbf{M}_t is in the local ENU frame, which is the same frame as the satellite elevation and azimuth angles. Then, \mathbf{M}_t can be used in satellite visibility classification, as shown in the next section.

4. GNSS PSEUDORANGE MEASUREMENT RECTIFICATION BASED ON SWM

From the measurements obtained from the GNSS receiver, each pseudorange measurement, ρ_n , can be described as follows [45]:

$$\rho_n = R_n + c(\delta t^r - \delta t_n^{sv}) + I_n + T_n + e_n, \quad (3)$$

where R_n is the geometric range between the satellite and the GNSS receiver, δt_n^{sv} denotes the satellite clock bias, δt^r is the receiver clock bias, I_n is the ionospheric delay distance, T_n is the tropospheric delay distance, and e_n represents the errors caused by factors such as multipath effects, NLOS receptions, receiver noise, and antenna delay. In a sparse area, e_n is small, and a small value can effectively bound the error caused by multipath and NLOS receptions. However, e_n can change dramatically in dense urban areas, and a fixed value cannot bound the error caused by GNSS signal reflections from the surroundings.

Recently, the work in [46] described a state-of-the-art general online sensor model validation and estimation framework. The framework consists of three parts: model validation, model calibration, and model repair. The authors propose that sensor measurements should be validated, calibrated or repaired before its integration with data from other sensors. The main reason behind this is that sensor measurements can be affected or polluted by environmental conditions, causing violations of the assumptions of the original sensor model. Many sensor measurements can violate the assumptions of the standard sensor model in challenging environments, such as urban canyons. For example, LiDAR-based positioning can be severely degraded in an urban canyon with numerous dynamic objects [47]. Therefore, a fixed sensor model cannot bound the potential error of LiDAR-based positioning. Therefore, the ability to effectively validate, calibrate and repair the sensor model as required is valuable for sensor fusion in such areas. Following the framework proposed by Jurado and Raquet [46], we applied the three phases to the GNSS pseudorange measurements (Fig. 4). First, model validation (Model 1 in Fig. 4) was performed based on satellite visibility classification using SWM. Second, if one satellite is classified as NLOS, we proceed to the model calibration phase, which re-estimates the GNSS measurement by correcting the NLOS pseudorange measurements. However, if one satellite is classified as NLOS, but its reflecting point is not found inside the SWM, which means NLOS correction is not available, we proceed to the model repair phase (Model 3 in Fig. 4) by de-weighting the NLOS measurements for use in further positioning. The remainder of this section describes these three phases.

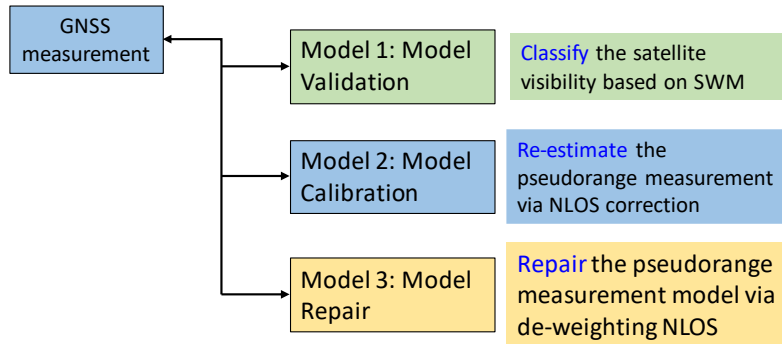


Fig. 4. Application of the framework proposed by Jurado and Raquet [46] to GNSS measurements before their use in the integration system. Three phases are included: model validation, model calibration, and model repair

4.1 Model Validation: NLOS Detection Based on SWM

In this section, we describe the details of NLOS detection based on the SWM generated as discussed in Section 3. Unlike the 3D building models, which consist of consistent surfaces from buildings [41], the SWM only provides unorganized discrete points. To effectively classify satellite visibility based on the SWM, we developed a fast searching method (Algorithm 1). The inputs of the algorithm include the SWM \mathbf{M}_t , elevation angle $\varepsilon_{t,i}$ of satellite i , the azimuth angle $\alpha_{t,i}$ of satellite i at epoch t , the maximum searching distance, D_{thres} , and a constant incremental value, Δd_{pix} . The output is the satellite visibility, $\mathbf{Vis}_{t,i}$, of satellite i . In Step 1, a search point is initialized at $(x_{L,t}^c, y_{L,t}^c, z_{L,t}^c)$, the center of the 3D LiDAR. A search direction connecting the GNSS receiver and the satellite is determined based on the elevation and azimuth angle of satellite i . The SWM is transformed into a $kdTree$ structure [48], $\mathbf{M}_{t,tree}$, for finding neighboring points. The $kdTree$ is a special structure for point cloud processing which

can perform efficiently when searching neighboring points. In Step 2, given a fixed incremental value, Δd_{pix} , the search point is moved to the next point $(x_{L,t,k}^s, y_{L,t,k}^s, z_{L,t,k}^s)$ calculated using (4)-(6), based on the search direction shown on the left-hand side of Figure 5. The number (N_k) of neighboring points near the search point is counted using the *kdTree* structure [48]. If N_k exceeds a certain threshold, there are some map points from buildings or dynamic objects near the search point $(x_{L,t,k}^s, y_{L,t,k}^s, z_{L,t,k}^s)$, and we consider that the line-of-sight connecting the GNSS receiver and satellite is blocked. Therefore, satellite i is classified as an NLOS satellite. Otherwise, repeat Steps 2 and 3. If $k\Delta d_{\text{pix}} > D_{\text{thres}}$, it means that the direction between the GNSS receiver and the satellite is line-of-sight. In this work, D_{thres} was set to 250 meters, so points within 250 meters were considered for NLOS detection. Only the direction connecting the GNSS receiver and the satellite needs to be considered, instead of traversing the whole SWM, an approach that contributes to the efficiency of NLOS detection. A satellite visibility classification result is shown on the right-hand side of Fig. 5. The red and blue circles represent the NLOS and LOS satellites, respectively. The length of the white line connecting the center of 3D LiDAR and the satellite is D_{thres} . Therefore, satellite visibility can be classified using Algorithm 1. In our implementation, less than 10 ms was spent on classifying the visibility of each satellite.

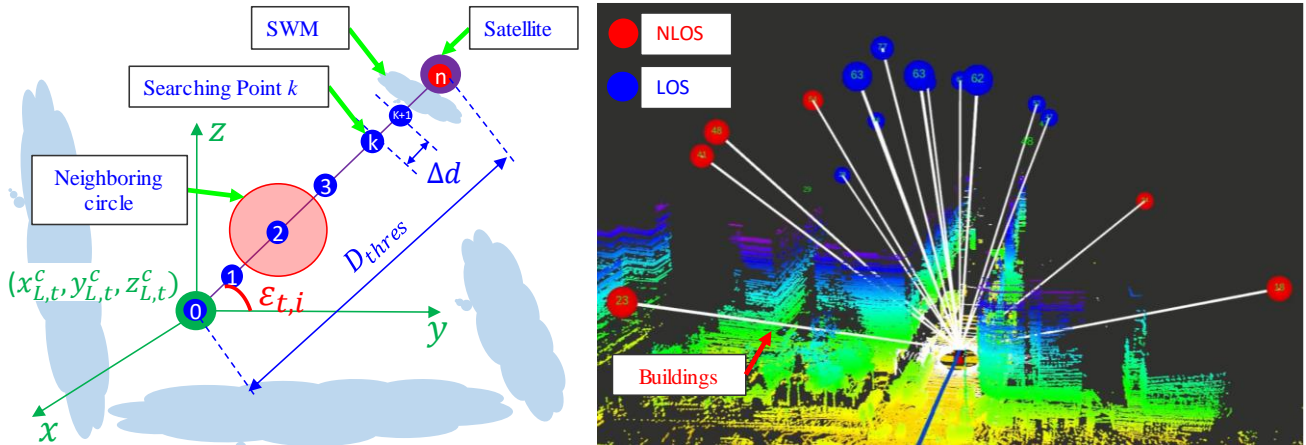


Fig. 5. Illustration of NLOS detection based on SWM. A detailed video can be found [here](#)

Algorithm 1: NLOS Detection based on SWM

Inputs: Point clouds $\mathbf{M}_t, \varepsilon_{t,i}, \alpha_{t,i}$.

Outputs: Satellite visibility $\mathbf{Vis}_{t,i}$

Step 1: Initialize the searching point at $(x_{L,t}^c, y_{L,t}^c, z_{L,t}^c)$, the searching direction denoted by $\varepsilon_{t,i}$ and $\alpha_{t,i}$, transfer the \mathbf{M}_t into *kdTree* and get $\mathbf{M}_{t,\text{tree}}$

Step 2: Given a constant incremental value Δd_{pix} , the searching point is updated as follows:

$$x_{L,t,k}^s = x_{L,t,k-1}^s + \Delta d_{\text{pix}} \sin(\alpha_{t,i}) \cos(\varepsilon_{t,i}) \quad (4)$$

$$y_{L,t,k}^s = y_{L,t,k-1}^s + \Delta d_{\text{pix}} \cos(\alpha_{t,i}) \cos(\varepsilon_{t,i}) \quad (5)$$

$$z_{L,t,k}^s = z_{L,t,k-1}^s + \Delta d_{\text{pix}} \sin(\varepsilon_{t,i}) \quad (6)$$

Step 3: if $k\Delta d_{\text{pix}} < D_{\text{thres}}$, find the nearest neighbor points (NNPs) of a given point $(x_{L,t,k}^s, y_{L,t,k}^s, z_{L,t,k}^s)$ and get N_k NNPs.

Step 4: Repeat Step 2~3, until $N_k > N_{\text{thres}}$. Then the satellite is NLOS ($\mathbf{Vis}_{t,i}=0$), else LOS ($\mathbf{Vis}_{t,i}=1$)

The numbers inside the circles on the right-hand side of Fig. 5 denote the elevation angle of the corresponding satellite. We can see that the NLOS satellite with an elevation angle of 54 degrees was detected. As shown in Fig. 2, the maximum mask elevation angle can reach 76 degrees. In practice, the maximum mask elevation angle based on SWM was significantly correlated with the width of the street. The narrower the street was, the higher the mask elevation angle is achieved. Although the proposed SWM has effectively enhanced the FOV of LiDAR sensing compared with our previous work described in [5, 9, 38, 39], the SWM still could not fully reconstruct scenarios with very tall buildings. However, according to recent research described in [9], NLOS satellites with low elevation angles produce the majority of GNSS positioning error.

4.2 Model Calibration: NLOS Correction Based on SWM

This section presents the details of NLOS correction (model calibration) based on an SWM (Fig. 4). The typical NLOS error model proposed in [4] is shown in Fig. 6. The expected signal transmission route is expressed as a dashed blue line in Fig. 6. The distance from the receiver to the building is represented by τ . The elevation angle of the GNSS signal is represented by θ_{ele} . We assume that:

- (1) The surrounding buildings and dynamic objects which can cause potential NLOS receptions are vertical.
- (2) GNSS signal reflections satisfy the law of reflection.
- (3) The NLOS signals are reflected only once.

Thus, we can get $\theta_a = \theta_b$. Moreover, the direction of real signal transmission is parallel to the direction of expected signal transmission. Finally, we have $\theta_a = \theta_b = \theta_0 = \theta_{ele}$. The route distance difference, γ , between the reflected signal and the expected signal is as follows:

$$\gamma = \gamma_1 + \gamma_2 \quad (7)$$

$$\gamma_1 = \tau \sec \theta_{ele} \quad (8)$$

$$\gamma_2 = \gamma_1 \cos(2\theta_{ele}) \quad (9)$$

Thus, NLOS error can be calculated based on the azimuth angle, elevation angle, and the distance from the receiver to the building causing the reflection. In general, two steps are needed to proceed with NLOS correction: NLOS detection (presented in Section 4.1) and NLOS error calculation based on the detected reflector. When correcting for NLOS satellites, the major difficulties lie in finding the reflectors which reflect the GNSS signals, to further estimate the distance between the GNSS receiver and the reflector.

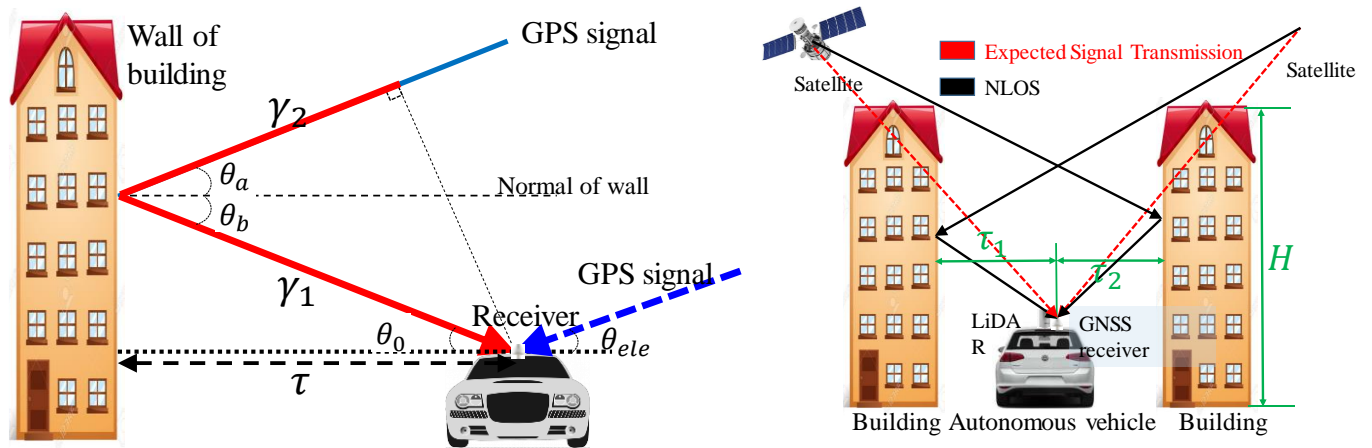


Fig. 6. Illustration of the NLOS error model and NLOS signal transmission route. The signal is reflected by the building and subsequently received by the receiver [4]

A ray-tracing [49] technique is commonly used to simulate NLOS signal transmission routes for finding the NLOS reflectors in range-based 3DMA GNSS [15-18]. This approach can incur a high computational load. However, unlike the 3D building models, the SWM described in this paper does not produce continuous building surfaces and clear building boundaries. The SWM only provides large amounts of dense, discrete, unorganized point clouds; there are about 10 million points inside an SWM. Instead of applying the ray-tracing technique to find the reflectors inside the SWM, we directly search for the reflectors from the SWM, using an efficient *kdTree* structure.

The details of the reflector detection algorithm are presented in Algorithm 2. The inputs of the algorithm include the point clouds \mathbf{M}_t , the elevation angle at epoch t for NLOS satellite i ($\epsilon_{t,i}$), the azimuth angle at epoch t for NLOS satellite i ($\alpha_{t,i}$), and the azimuth resolution, α_{res} , as in Algorithm 1. The output is the closest reflecting point, p_r^s , which is the most probable reflector for NLOS satellite i .

Step1. A search point is initialized at the center of the 3D LiDAR. The search direction is determined based on the satellite elevation, $\epsilon_{t,i}$, and α_s . The SWM is transformed into a *kdTree* structure for use in the neighbor search, as in Algorithm 1. **Step2.** Based on the assumption that $\theta_a = \theta_{ele}$ [19], the reflected signal should have the same elevation angle as the expected directed

signal (Fig. 6). Therefore, we traverse all the azimuths from 0 to 360 degrees, with an azimuth resolution of α_{res} and elevation angle of $\varepsilon_{t,i}$, to find all the possible routes of NLOS transmissions. For example, for a given direction specified by $\varepsilon_{t,i}$ and α_s , the line-of-sight between the GNSS receiver and satellite is identified based on Algorithm 1. **Step3**. If the line-of-sight is blocked by a point, p_j , (Step 2 in Algorithm 2) and the line-of-sight connecting the point p_j and the satellite i is not blocked (Step 3 in Algorithm 2), point p_j is considered as a possible reflector and is saved to \mathbf{Q}_t . **Step 4**. The α_s proceed to the next azimuth based on Step 4. By repeating Steps 2 and 3, all possible reflectors are identified, based on the assumption that $\theta_a = \theta_{ele}$. Fig. 7 (a)-(d) shows the result of possible reflector detection for 1-2 NLOS satellites. We observe that multiple possible reflectors are found using Steps 1 to 4. The red circles in Fig. 7 denote the NLOS satellite, and the red lines denote possible NLOS reflection and transmission routes. According to [4], the reflector with the shortest distance is usually the best candidate. **Step 5**. A unique reflector can be detected based on the shortest distance assumption (Step 5), as shown in Fig. 7 (e). Therefore, the reflecting point for a given satellite i is detected as p_r^s , and the distance (τ) needed in formula (8) can be calculated accordingly.

Algorithm 2: Reflecting Point Detection (RPD) based on SWM

Inputs: Point clouds \mathbf{M}_t , $\varepsilon_{t,i}$, $\alpha_{t,i}$ and azimuth resolution as α_{res} .

Outputs: Reflecting point p_r^s .

Step 1: Initialize the searching point at $(x_{L,t}^c, y_{L,t}^c, z_{L,t}^c)$, the searching direction denoted by $\varepsilon_{t,i}$ and $\alpha_{t,i}$, transfer the \mathbf{M}_t into *kdTree* and get $\mathbf{M}_{t,tree}$. Initialize reflecting points array \mathbf{Q}_t . $\alpha_s = 0$.

Step 2: Get the first point p_j inside the map blocking the searching direction denoted by $\varepsilon_{t,i}$ and α_s using Algorithm 1. if p_j is found, go to Step 3, otherwise go to Step 4.

Step 3: If the direction connecting the point and satellite is visible, save p_j to \mathbf{Q}_t

Step 4: $\alpha_s = \alpha_s + \alpha_{res}$, repeat Step 1 to 2 until $\alpha_s > 360^\circ$.

Step 5: find the most likely reflector p_j from \mathbf{Q}_t with the shortest distance between the GNSS receiver and the reflector. Save p_j to p_r^s .

The proposed NLOS reflector detection method does not rely on the accuracy of the detection of building surfaces. The short distance assumption applied in Step 5 of Algorithm 2 can effectively prevent overcorrection, as only the closest reflector is identified as the unique reflector. Due to the sparsity of the SWM, although it is still denser than the 3D real-time point clouds, there are still some satellites whose reflectors cannot be found using the SWM. Therefore, we remodel NLOS satellites whose reflectors are not found, using the approach described in the next section, based on the framework shown in Fig. 4.

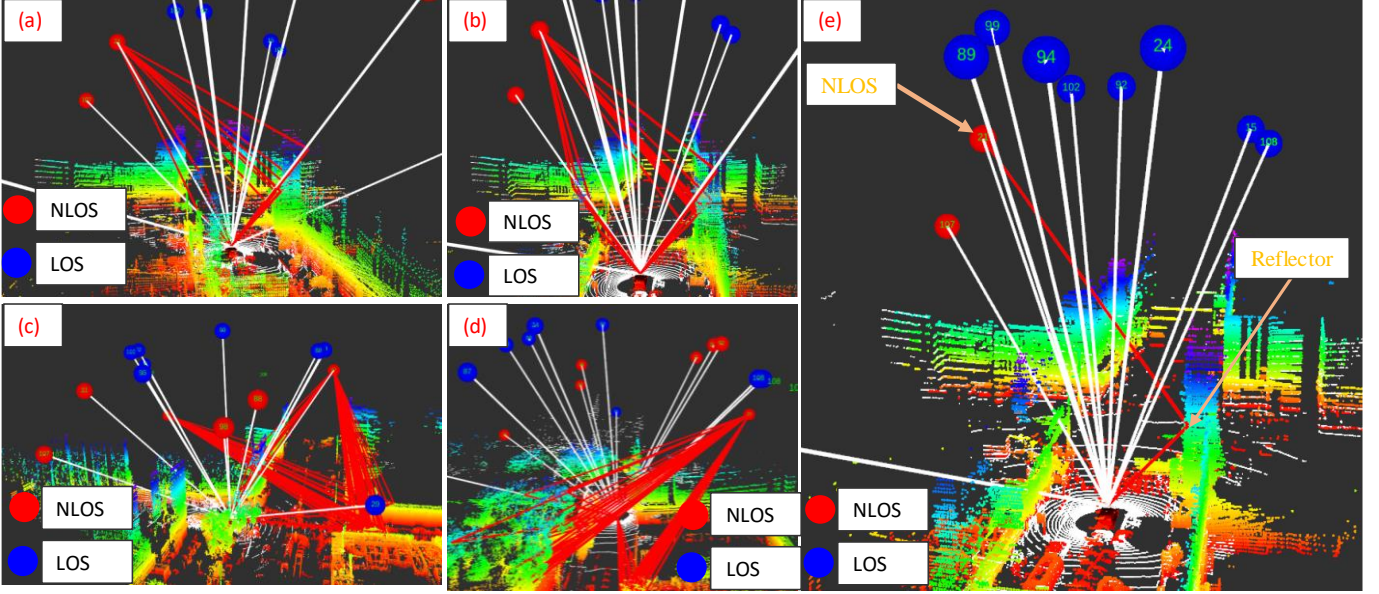


Fig. 7. Demonstration of the NLOS signal reflector detection. Red and blue circles represent NLOS and LOS satellites, respectively. White lines denote LOS transmission routes. Red lines represent NLOS transmission routes. Multiple possible NLOS transmission routes are shown in (a)-(d). The most probably NLOS transmission route is shown in (e), based on the shortest route assumption adopted in Algorithm 2

4.3 Model Repair: NLOS Remodeling

If the reflector for an NLOS satellite is not detected, we remodel it as described in this section, instead of simply excluding it (Fig. 4). According to [4], satellites with lower elevation angles and smaller signal to noise ratios (SNR) have a higher possibility of contamination by NLOS errors [4]. Pseudorange uncertainty modeling based on the satellite elevation angle and SNR was reported in [50, 51]. The weighting scheme in [51] produces satisfactory performance in open areas. However, the scheme may not work in dense urban areas, as the NLOS can have high elevation angles and SNR, as can be seen in our previous work [38]. This weighting scheme treats the LOS and NLOS in the same manner, which is not preferable when the NLOS has already been detected. The weighting scheme in [50] employs a scaling factor to assign the LOS and NLOS different weightings. Inspired by this approach, we modeled the uncertainty of LOS and NLOS using the weighting scheme described in [51]. A scaling factor was added onto the scheme to treat the LOS and NLOS differently. Assume that \mathbf{SV}_i represents the information from satellite i and $\mathbf{SV}_i = \{\varepsilon_i, \alpha_i, SNR_i, \rho_i\}$, α_i denotes the satellite azimuth angle, ε_i represents the satellite elevation angle, SNR_i indicates the satellite SNR, and ρ_i denotes the pseudorange measurement. The weighting scheme presented in [51] is as follows:

$$W_{LOS}^{(i)}(\varepsilon_i, SNR_i) = \frac{1}{\sin^2 \varepsilon_i} \left(10^{-\frac{(SNR_i - T)}{a}} \left(\left(\frac{A}{10^{\frac{(F-T)}{a}}} - 1 \right) \frac{(SNR_i - T)}{F - T} + 1 \right) \right) \quad (10)$$

The parameter T indicates the SNR threshold. Parameters a , A and F are experimentally determined. The weighting matrix W is a diagonal matrix constructed by the weighting $W^{(i)}(el_i, SNR_i)$. The weighting scheme treats LOS and NLOS using the same formula. We added a scaling factor, K , to adapt the weighting scheme to treat LOS and NLOS differently, as follows:

$$W_{NLOS}^{(i)}(el_i, SNR_i) = K \cdot W_{LOS}^{(i)}(el_i, SNR_i) \quad (11)$$

When the received signal is LOS, K is equal to 1. When the signal is NLOS, K changes, and is experimentally determined. In this work, the variance, σ_p , of a pseudorange measurement is computed as $\sigma_p = 1/W^{(i)}(el_i, SNR_i)$. In this case, satellite visibility is classified, and the corresponding uncertainty is modeled.

5. GNSS/INS INTEGRATION USING FACTOR GRAPH OPTIMIZATION

In general, the goal of the multi-sensor integration is to find the optimal posterior state given measurements from sensors. Therefore, the sensor integration problem can be formulated as a typical maximum *a posteriori* (MAP) problem [26]. In this paper, the measurements include two parts, the GNSS and INS measurements. Assuming that the GNSS and INS measurements are independent, we can formulate the GNSS/INS integration problem as:

$$\hat{\mathbf{X}} = \arg \max \prod_{t,i} P(\mathbf{z}_{t,i} | \mathbf{x}_t) \prod_t P(\mathbf{x}_t | \mathbf{x}_{t-1}, \mathbf{u}_t) \quad (12)$$

where $\mathbf{z}_{t,i}$ represents the GNSS raw measurements at epoch t , and \mathbf{x}_k represents the system state at epoch t . The index of measurements at a given epoch t is denoted as i , so one epoch can have multiple pseudorange measurements. The control input (INS measurements) is denoted by \mathbf{u}_t , and the optimal system state set is $\hat{\mathbf{X}}$ [26]. A conventional Bayes filter-based method finds the best estimation of the current state considering only the previous state and the control input and observation measurements at the current epoch. This approach fails to take full advantage of historical information. Conversely, FGO-based sensor integration [52] has been used to transfer the MAP problem into a non-linear optimization problem.

In FGO-based integration, all sensor measurements are treated as factors [52] associated with specific states [52]. According to [53], the MAP problem can be expressed as:

$$\begin{aligned} \hat{\mathbf{X}} &= \arg \max_{\mathbf{X}} (\prod_j \zeta_j(\mathbf{x}_j)) \\ &\text{with } \zeta_j(\mathbf{x}_j) \propto \exp(-\|h_j(\mathbf{x}_j) - \mathbf{z}_j\|_{\Sigma_j}^2), \end{aligned} \quad (13)$$

where $\zeta_j(\mathbf{x}_j)$ is a factor associated with the measurements \mathbf{z}_j , which can be derived from both GNSS and INS measurements. The Σ_j denotes the uncertainty associated with the given measurement \mathbf{z}_j . The state \mathbf{x}_j is associated with the measurements \mathbf{z}_j . An observation function, $h_j(*)$, is associated with \mathbf{z}_j . The state set that needs to be estimated is denoted $\mathbf{X} = \{\mathbf{x}_1, \mathbf{x}_2, \mathbf{x}_3, \dots, \mathbf{x}_k, \dots\}$. Assuming that all sensor noise has a Gaussian distribution, the negative logarithm of $\zeta_j(\mathbf{x}_j)$ is proportional to the error function [53] associated with the measurements. Therefore, Equation (20) can be transformed as follows:

$$\hat{\mathbf{X}} = \arg \min_{\mathbf{X}} (\prod_j \|h_j(\mathbf{x}_j) - \mathbf{z}_j\|_{\Sigma_j}^2) \quad (14)$$

The FGO transforms the (19) into a standard non-linear least squares problem, as shown in (21), and is used to obtain the optimal state set, \mathbf{X} , by minimizing the derived error function (14).

The graph structure of the GNSS/INS integration is shown in Fig. 8. The state-space of the system is represented as:

$$\mathbf{x}_t = (\mathbf{X}_{t,r}^{ecef}, \mathbf{V}_{t,r}^{ecef}, \mathbf{B}_{t,r}^{body}, \delta_{t,r}^{clock})^T, \quad (15)$$

where \mathbf{x}_t denotes the system state. Note that the \mathbf{x}_t here is different from that in Fig. 3. The position of the GNSS receiver in the ECEF coordinate [3] (denoted by the subscript, r) at given epoch t is represented by $\mathbf{X}_{t,r}^{ecef} = (x_{t,r}^{ecef}, y_{t,r}^{ecef}, z_{t,r}^{ecef})$. The velocities of the GNSS receiver in ECEF coordinate are denoted by $\mathbf{V}_{t,r}^{ecef} = (vx_{t,r}^{ecef}, vy_{t,r}^{ecef}, vz_{t,r}^{ecef})$, respectively. The bias of the accelerometer in the body (INS) frame is denoted by $\mathbf{B}_{t,ins}^{body} = (a_{t,x}^{body}, a_{t,y}^{body}, a_{t,z}^{body})$. The GNSS receiver clock bias is $\delta_{t,r}^{clock}$. In Fig. 8, the black-shaded rectangle represents the INS factor. The green- and red-shaded rectangles denote the LOS and NLOS satellite factors, respectively. The blue-shaded box represents the state transition factor.

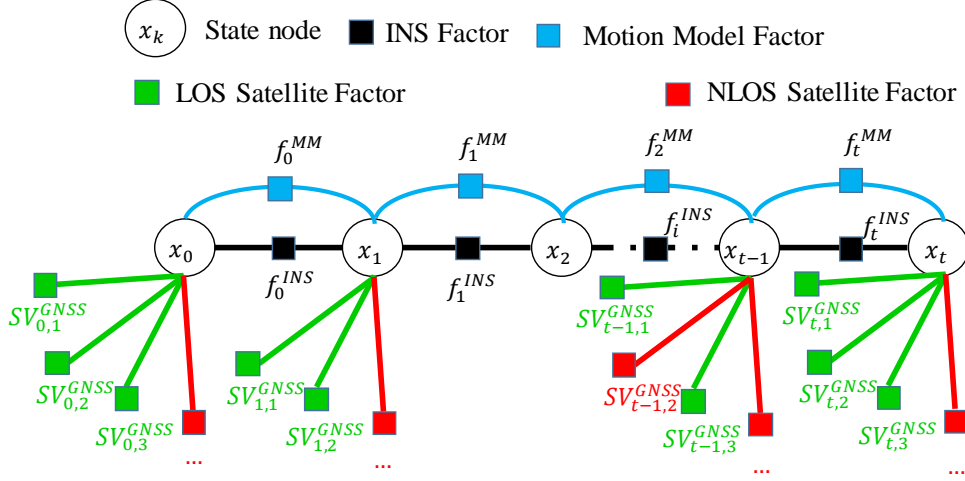


Fig. 8. Graph structure of tightly-coupled GNSS/INS integration using FGO

5.1 Motion Model Factor

We used a constant velocity model [54] to constrain the two consecutive states. Based on the constant velocity model, the motion model can be expressed as:

$$\mathbf{x}_t = h^{MM}(\mathbf{x}_{t-1}) + N(0, \Sigma_t^{MM}), \quad (16)$$

where $h^{MM}(\ast)$ represents the motion model function. Based on the constant velocity motion model, the motion model function can be expressed as follows:

$$h^{MM}(\mathbf{x}_{k-1}) = \begin{bmatrix} x_{t-1,r}^{ecef} + vx_{t-1,r}^{ecef} \cdot \Delta t \\ y_{t-1,r}^{ecef} + vy_{t-1,r}^{ecef} \cdot \Delta t \\ z_{t-1,r}^{ecef} + vz_{t-1,r}^{ecef} \cdot \Delta t \\ \mathbf{B}_{t-1,ins}^{body\ T} \\ \boldsymbol{\delta}_{t-1,r}^{clock} \end{bmatrix}, \quad (17)$$

where Δt is the time difference between the two states. The covariance matrix associated with the motion model is Σ_t^{MM} . Therefore, the error function (\mathbf{e}_t^{MM}) of the motion model factor can be expressed as:

$$\|\mathbf{e}_t^{MM}\|_{\Sigma_t^{MM}}^2 = \|\mathbf{x}_t - h^{MM}(\mathbf{x}_{t-1})\|_{\Sigma_t^{MM}}^2 \quad (18)$$

5.2 INS Factor

we make use of only the raw linear acceleration (\mathbf{A}_t^{raw}) and the attitude ($\mathbf{R}_{LB,t}$) from the AHRS. Therefore, the measurement from the accelerometer is expressed as follows:

$$\mathbf{A}_t^{raw} = (ax_t^{body}, ay_t^{body}, az_t^{body})^T, \quad (19)$$

where ax_t^{body} , ay_t^{body} , and az_t^{body} represent the acceleration measurements in the body frame. As the estimated state, \mathbf{x}_t , is in the global frame (ECEF), we need to transform the acceleration measurements from the body frame to the global frame based on the orientation and its position in the last epoch. The transformed acceleration measurements $\mathbf{A}_t^{ecef} = (ax_t^{ecef}, ay_t^{ecef}, az_t^{ecef})^T$ are as follows [3]:

$$\mathbf{A}_t^{ecef} = \mathbf{R}_{GL,t} \mathbf{R}_{LB,t} (\mathbf{A}_t^{raw} - \mathbf{B}_{t,ins}^{body}), \quad (20)$$

where $\mathbf{R}_{LB,t}$ is the transformation matrix used to transform the acceleration measurements from the body to the local frames, and can be expressed as follows:

$$\begin{aligned} \mathbf{R}_{LB,t} &= \mathbf{R}_{LB}^z(\alpha)\mathbf{R}_{LB}^y(\beta)\mathbf{R}_{LB}^x(\gamma) \\ \text{with } \mathbf{R}_{LB}^z(\alpha) &= \begin{bmatrix} \cos(\alpha) & -\sin(\alpha) & 0 \\ \sin(\alpha) & \cos(\alpha) & 0 \\ 0 & 0 & 1 \end{bmatrix} \\ \mathbf{R}_{LB}^y(\beta) &= \begin{bmatrix} \cos(\beta) & 0 & \sin(\beta) \\ 0 & 1 & 0 \\ -\sin(\beta) & 0 & \cos(\beta) \end{bmatrix} \\ \mathbf{R}_{LB}^x(\gamma) &= \begin{bmatrix} 1 & 0 & 0 \\ 0 & \cos(\gamma) & -\sin(\gamma) \\ 0 & \sin(\gamma) & \cos(\gamma) \end{bmatrix} \end{aligned} \quad (21)$$

where α , β , and γ denote the yaw, pitch and roll angles, respectively. The rotation matrices corresponding to the yaw, pitch, and roll angles are denoted $\mathbf{R}_{LB}^z(\alpha)$, $\mathbf{R}_{LB}^y(\beta)$ and $\mathbf{R}_{LB}^x(\gamma)$, respectively. The transformation matrix used to transform the acceleration measurements from the local frame to the global frame based on the \mathbf{x}_k is denoted $\mathbf{R}_{GL,t}$ and can be expressed as follows:

$$\mathbf{R}_{GL} = \begin{bmatrix} -\sin(\varphi_{lon}) & -\sin(\varphi_{lat})\cos(\varphi_{lon}) & \cos(\varphi_{lat})\cos(\varphi_{lon}) \\ \cos(\varphi_{lon}) & -\sin(\varphi_{lat})\sin(\varphi_{lon}) & \cos(\varphi_{lat})\sin(\varphi_{lon}) \\ 0 & \cos(\varphi_{lat}) & \sin(\varphi_{lat}) \end{bmatrix}, \quad (22)$$

where φ_{lon} and φ_{lat} represent the longitude and latitude based on the WGS84 geodetic system [3], which can be derived from \mathbf{x}_k . The measurement model for the linear acceleration is as follows:

$$\mathbf{x}_t = h^{INS}(\mathbf{x}_{t-1}, \mathbf{A}_t^{ecef}) + N(0, \Sigma_t^{INS}), \quad (23)$$

with the measurement function $h^{INS}(\mathbf{x}_{t-1}, \mathbf{A}_t^{ecef})$ as follows:

$$h^{INS}(\mathbf{x}_{t-1}, \mathbf{A}_t^{ecef}) = \begin{bmatrix} vx_{t-1,r}^{ecef} + ax_t^{ecef} \cdot \Delta t \\ vy_{t-1,r}^{ecef} + ay_t^{ecef} \cdot \Delta t \\ vz_{k-1,r}^{ecef} + az_k^{ecef} \cdot \Delta t \end{bmatrix}, \quad (24)$$

where the covariance matrix for the INS factor is Σ_k^{INS} . We can formulate the error function for INS acceleration measurements as follows:

$$\|\mathbf{e}_t^{INS}\|_{\Sigma_t^{INS}}^2 = \|\mathbf{x}_t - h^{INS}(\mathbf{x}_{t-1}, \mathbf{A}_t^{ecef})\|_{\Sigma_t^{INS}}^2, \quad (25)$$

where Σ_t^{INS} is constant, and is based on the specification of INS.

5.3 GNSS Pseudorange Factor

The GNSS pseudorange measurements, \mathbf{SV}_t , include the healthy pseudorange, \mathbf{SV}_t^C , the re-modeled pseudorange, \mathbf{SV}_t^M , and the corrected pseudorange, \mathbf{SV}_t^C at epoch t can be expressed as follows:

$$\mathbf{SV}_t = \{\mathbf{SV}_{t,1}, \mathbf{SV}_{t,2}, \dots, \mathbf{SV}_{t,i}, \dots, \mathbf{SV}_{t,N}\} \quad (26)$$

The position of the GNSS receiver is $\mathbf{x}_{t,r}^{ecef} = (x_{t,r}^{ecef}, y_{t,r}^{ecef}, z_{t,r}^{ecef})$. The position of a satellite $\mathbf{SV}_{t,i}$ is represented by $\mathbf{x}_{SV,i}^{xyz} = (x_{SV,i}^{ecef}, y_{SV,i}^{ecef}, z_{SV,i}^{ecef})^T$. Therefore, we can obtain the predicted GNSS pseudorange measurement for satellite $\mathbf{SV}_{t,i}$ as:

$$h^p(\mathbf{SV}_{t,i}, \mathbf{x}_{t,r}^{ecef}, \delta_{t,r}^{clock}) = \|\mathbf{x}_{SV,i}^{xyz} - \mathbf{x}_{t,r}^{ecef}\| + \delta_{t,r}^{clock}, \quad (27)$$

where $h^p(*)$ is the measurement function of the pseudorange. In this work, the earth rotation and atmospheric delay were calculated in advance using the model detailed in [51]. The measured pseudorange from the GNSS receiver is expressed as $\rho_{SV,i}$ and is given by $h^p(\mathbf{SV}_{t,i}, \mathbf{X}_{t,r}^{ecef}, \delta_{t,r}^{clock})$ with additional Gaussian noise. We have the following formulation:

$$\rho_{SV,i} = h^p(\mathbf{SV}_{t,i}, \mathbf{X}_{t,r}^{ecef}, \delta_{t,r}^{clock}) + N(0, \Sigma_{t,i}^{SV}), \quad (28)$$

where $\Sigma_{t,i}^{SV}$ is the uncertainty of the satellite measurement $\rho_{SV,i}$. We can calculate the error function for a given satellite measurement, $\rho_{SV,i}$, as follows:

$$\|\mathbf{e}_{t,i}^p\|_{\sigma_p^2}^2 = \|\rho_{SV,i} - h^p(\mathbf{SV}_{t,i}, \mathbf{X}_{t,r}^{ecef}, \delta_{t,r}^{clock})\|_{\Sigma_{t,i}^{SV}}^2 \quad (29)$$

5.4 Efficient Incremental Optimization

In this section, we formulate three kinds of factors including the motion model factor, the INS (accelerometer) factor, and the GNSS pseudorange factor. The optimal state set \mathbf{X} can be solved as follows:

$$\mathbf{X}^* = \arg \min_{\mathbf{X}} \sum_{i,k} \|\mathbf{e}_{t,i}^p\|_{\Sigma_{t,i}^{SV}}^2 + \|\mathbf{e}_t^{MM}\|_{\Sigma_t^{MM}}^2 + \|\mathbf{e}_t^{INS}\|_{\Sigma_t^{INS}}^2 \quad (30)$$

To solve the optimization problem, we used ISAM2 [53] in GTSAM [55].

6. EXPERIMENTAL RESULTS AND DISCUSSION

6.1 Experimental Setup

Two experiments were conducted in typical urban canyons in Hong Kong on 12 October 2019 (Fig. 9). The figure on the left shows the test vehicle with all the sensors installed in a compact sensor kit. The middle and right figures show the urban canyons used. Both of the urban scenarios contain static buildings, trees and dynamic objects, such as double-decker buses and cars. We are aware of the limitation of the method described in this paper, mentioned at the end of Section 4.1, that the sliding window map cannot sense the roof of buildings above 40 meters high in dense urban environments. We first carried out the experiment in a typical urban canyon in Hong Kong (Urban Canyon 1 in Fig. 9). Then we performed another experiment in a highly urbanized area in Hong Kong (Urban Canyon 2 in Fig. 9), in which the buildings are significantly higher, and which is one of the densest areas in Hong Kong, to study the limitations of the proposed method. Some NLOS satellites reflected by buildings taller than 40 meters may not be detected using SWM. In both experiments, a u-blox M8T GNSS receiver was used to collect raw GPS/BeiDou measurements at a frequency of 1 Hz. A 3D LiDAR sensor (Velodyne 32) was employed to collect raw 3D point clouds at a frequency of 10 Hz. The Xsens Ti-10 IMU was employed to collect data at a frequency of 100 Hz. In addition, the NovAtel SPAN-CPT, a GNSS (GPS, GLONASS, and Beidou) RTK/INS (fiber-optic gyroscopes, FOG) integrated navigation system was used to provide ground truth of positioning. The gyro bias in-run stability of the FOG is 1 degree per hour, and its random walk is 0.067 degrees per hour. The baseline between the rover and the GNSS base station is about 7 km. All the data were collected and synchronized using a robot operation system (ROS) [56]. The coordinate systems between all the sensors were calibrated before the experiments. The experimentally determined parameters used in this paper are shown in Table I.

Table 1. Parameter values used

Parameters	N_{sw}	Δd_{pix}	α_{res}	N_{thres}
Values	50	2	1°	10
Parameters	K	a	A	F
Values	1.65	30	32	10

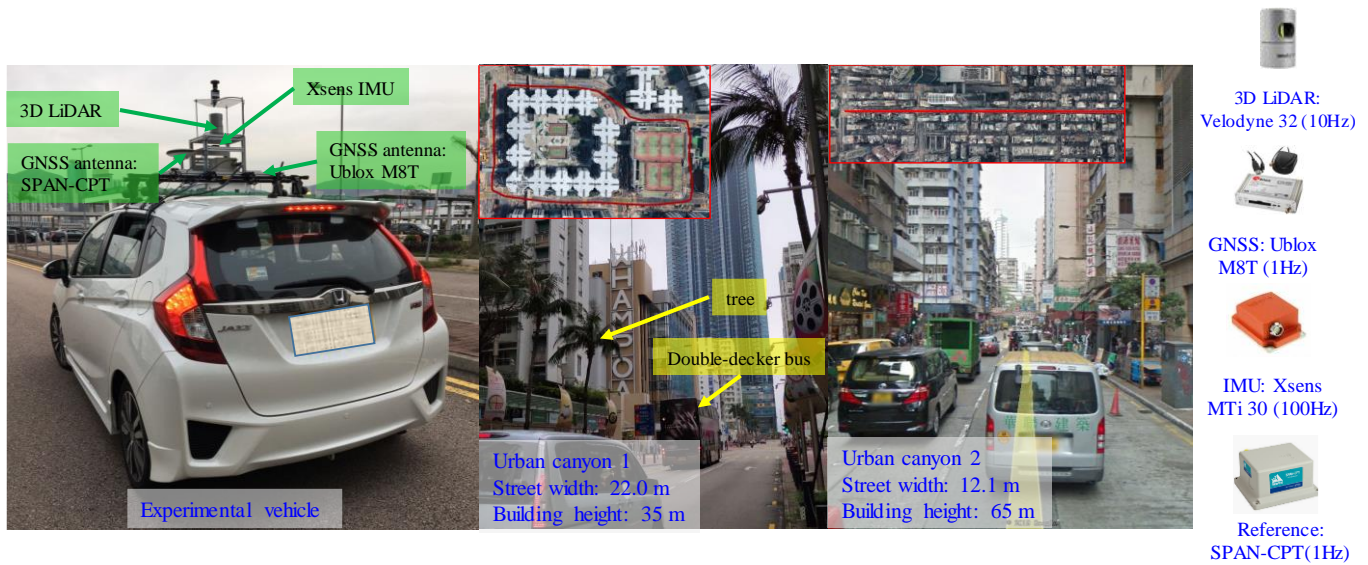


Fig. 9. Experimental vehicle and tested scenarios of Urban Canyons 1 and 2

We first analyzed the performance of GNSS standalone positioning by comparing five single point positioning (SPP) methods, as shown below. The objective of this analysis was to validate the effectiveness of the proposed method in improving the GNSS standalone positioning.

- u-blox**: the GNSS positioning solution from the u-blox M8T receiver.
- WLS**: weighted least squares (WLS) method [51].
- WLS-NE**: weighted least squares (WLS) method [51] with all NLOS satellites excluded.
- R-WLS**: WLS method with the aid of the re-weighting scheme in equation (11); all NLOS satellites were re-weighted.
- CR-WLS** (proposed SPP): WLS method with the aid of (1) the NLOS correction proposed in Section 4.2 if the reflector was detected, and (2) the re-weighting scheme in equation (11) if the reflector was not detected.

Three GNSS/INS integrated positioning methods were also compared:

- EKF**: Standard EKF-based tightly coupled GNSS/INS integration based on [57].
- FG**: Factor graph-based tightly-coupled GNSS/INS integration[39].
- FG-3DLA** (proposed integration): Factor graph-based tightly coupled GNSS/INS integration with the help of 3D LiDAR aided GNSS, as described in this paper.

6.2 Evaluation of Urban Canyon 1 Experiment

6.2.1 GNSS Standalone Positioning

The results of the GNSS standalone positioning experiments using the five methods are shown in Table 2. The first column shows the 2D positioning error of the u-blox receiver. The positioning result is based on standard NMEA [3] messages from the u-blox receiver. A mean error of 31.02 meters was obtained, with a standard deviation of 37.69 meters. The maximum error reached 177.59 meters due to excessive reflections from surrounding buildings. The GNSS solution was available throughout the experiment. The second column shows the positioning result using the raw pseudorange measurements from the u-blox receiver and positioning based on WLS. The weighting scheme was taken from [51] and is based on the satellite elevation angle and the signal to noise ratio (SNR). The positioning error decreased to 9.57 meters with a standard deviation of 7.32 meters. The maximum error also decreased to less than 50 meters. Based on the NLOS detection results shown in Section 4.1, the positioning error increased to 11.63 meters after excluding all detected NLOS satellites, a result that is even worse than that of the WLS. This situation arose because excessive NLOS exclusion can significantly distort the perceived geometric distribution of the satellites. Our previous results, described in [9, 38], showed a similar phenomenon. The standard deviation also increased compared with that of the WLS. Availability decreased slightly from 100% (WLS) to 96.01%. Complete NLOS exclusion is therefore not preferable in urban canyons. The fourth column of the table presents the results of R-WLS where all the NLOS satellites were remodeled based on the weighting scheme described in Section 4.3, instead of excluding the NLOS satellites detected. The 2D mean error was reduced from 9.57 meters (WLS) to 9.01 meters. Both the standard deviation and maximum errors decreased slightly. The last column shows the 2D positioning error of CR-WLS. The 2D positioning error decreased to 7.92 meters, with a standard deviation of 5.27 meters. Availability is also guaranteed using the proposed method (CR-WLS).

The improved GNSS standalone positioning results demonstrate the effectiveness of the proposed method in mitigating the effects of NLOS signals.

Table 3 depicts the accuracy of NLOS satellite detection. As mentioned in Section 4.1, the proposed SWM cannot fully construct all environments, so some NLOS satellites with high elevation angles cannot be detected. Therefore, we evaluated the NLOS detection performance at three elevation angle ranges. The second row in Table 3 shows the percentage of NLOS satellites that belonged to a certain elevation angle range. The NLOS satellites with elevation angles between 0° and 30° made up 43.8% of all NLOS satellites. Of these NLOS satellites, 92% were detected using the method described in Section 4.1. The NLOS detection accuracy for NLOS satellites (28.9%) with elevation angles between 30° and 60° was 35%. Similar NLOS detection accuracy (27.35%) was obtained for NLOS satellites with elevation angles between 60° and 90° . Although the NLOS satellites with high elevation angles were not detected effectively, the proposed method is a new and general solution for NLOS detection. Due to the decreased cost of 3D LiDARs, multiple 3D LiDARs [58] is a common sensor setup for safety-critical ADV, to guarantee robustness. The use of multiple 3D LiDARs can significantly enhance the FOV of the proposed SWM. Therefore, NLOS satellites with high elevation angles can be detected by autonomous driving vehicles using multiple 3D LiDARs [58].

Table 2. Positioning performance of GNSS SPP in Urban Canyon 1

GNSS Positioning	u-blox	WLS	WLS-NE	R-WLS	CR-WLS
Mean error	31.02 m	9.57 m	11.63 m	9.01 m	7.92 m
Std	37.69 m	7.32 m	13.05 m	6.90 m	5.27 m
Maximum error	177.59 m	46.29 m	52.93 m	43.59 m	41.75 m
Availability	100 %	100%	96.01 %	100%	100%

Table 3. Performance of NLOS classification between different elevation ranges in Urban Canyon 1

All data	Elevation (0° – 30°)	Elevation (30° – 60°)	Elevation (60° – 90°)
Percentage of NLOS Satellites	43.8 %	28.9%	27.35 %
Accuracy of NLOS Detection at Different Elevation Angles	92 %	35 %	21%

Tables 4 and 5 show the values of NLOS correction using the proposed method in two selected epochs. In Table 4, NLOS satellite 8, with an elevation angle of 23.49° and C/N_0 of 15 dB-Hz, was detected and the NLOS correction was 10.08 meters. The fourth column shows the exact NLOS delay, labeled using a ray-tracing technique [15] based on ground truth positioning provided by the reference system SPAN-CPT. We can see that the exact NLOS delay (15.55 meters) was slightly larger than the NLOS delay estimated using the proposed method. The major reason for the difference is that the proposed method finds the reflectors based on the shortest distance assumption. Therefore, the reflector may not be perfectly detected. In general, we find that NLOS satellites with lower elevation angles usually cause larger NLOS delay, as shown in column four of Table 4. The other epoch data shown in Table 5 show a slightly different trend. Satellite 30, with an elevation angle of 56.22 degrees, caused the largest NLOS delay, of 48.52 meters. According to (7) and Fig. 6, NLOS delay is determined by the elevation angle and the distance between the GNSS receiver and the reflector. The main reason for the large NLOS delay caused by satellite 30 is the long distance between the GNSS receiver and the reflector. The majority of NLOS satellites were detected and corrected using the proposed method. Fig. 10 shows a case in which the NLOS satellites were blocked by a traffic signal pole instead of 3D buildings. Conventionally, the 3DMA GNSS only considers static buildings. However, infrastructure such as traffic signal pole and even guard bars can also cause NLOS receptions. Satellites 7, 99 and 112 were all blocked by the signal pole. With increased complexity and density of infrastructure [59], which is not included in conventional 3D building models, NLOS receptions caused by such structures should also be considered. We believe that this is a significant contribution of the proposed method.

Table 4. NLOS pseudorange correction in Urban Canyon 1 (Epoch 33661)

Satellite PRN	Elevation Angle (degree)	C/N_0 (dB-Hz)	Actual Pseudorange Correction (ground truth)	Estimated Pseudorange Correction
8	23.49	15	15.55 m	10.08 m
17	23.13	18	13.73 m	8.14 m
11	62.45	24	3.87 m	7.59 m

Table 5. NLOS pseudorange correction in Urban Canyon 1 (Epoch 33730)

Satellite PRN	Elevation Angle (degree)	C/N ₀ (dB-Hz)	Actual Pseudorange Correction (ground truth)	Estimated Pseudorange Correction
22	26.91	19	12.02 m	10.17 m
28	28.60	18	16.41 m	9.47 m
30	56.22	30	48.52 m	27.31 m

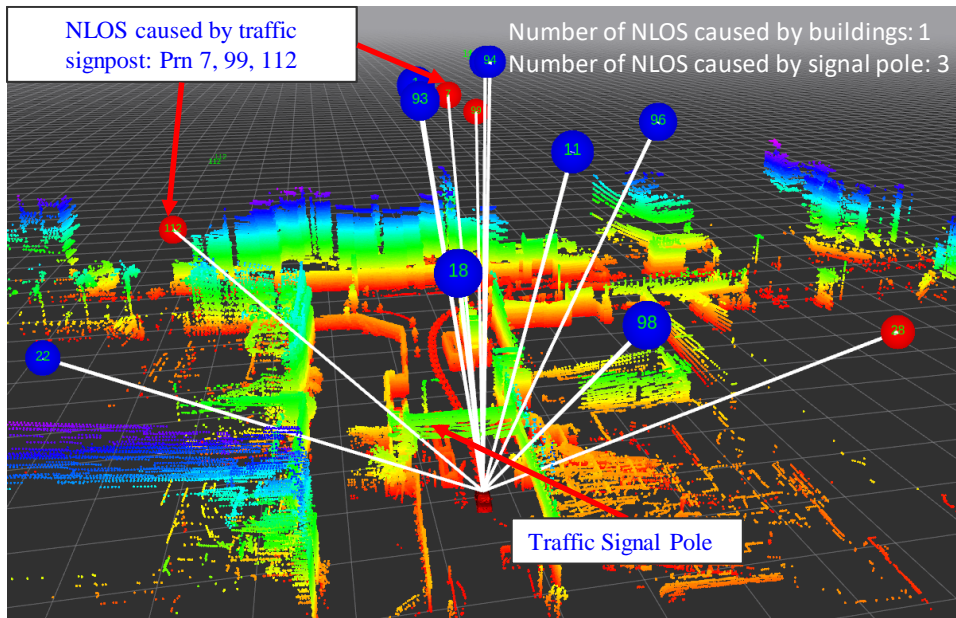


Fig. 10. Illustration of NLOS receptions blocked by an overhead traffic signal pole instead of 3D buildings. The blue and red circles denote the LOS and NLOS satellites, respectively. The numbers inside the circles denote the satellite PRN

In short, the best performance of GNSS standalone positioning was obtained using CR-WLS. These improved results show that the proposed method can mitigate the effects of NLOS receptions by remodeling and correcting NLOS signals. Due to the complementarity of GNSS and INS, the remodeling and correction of GNSS measurements can contribute to the GNSS/INS integration.

6.2.2 GNSS/INS Integrated Positioning

In this section, we present the results of GNSS/INS integration. Table 6 shows the 2D positioning errors identified using the three kinds of GNSS/INS integration listed. A 2D mean error of 8.03 meters was obtained using EKF, with a maximum error of 44.55 meters. Significantly improved positioning accuracy was obtained after the application of the state-of-the-art FGO, with the mean error decreasing from 8.03 to 3.64 meters. Both the standard deviation and the maximum error decreased. Our recent research, described in [39], extensively evaluated the performance of GNSS/INS integration using EKF and factor graphs. The improvement caused by the factor graph is due to the iteration and re-linearization employed during factor graph optimization [39]. Unlike conventional EKF based GNSS/INS integration, the FGO makes use of historical measurements during optimization, which exploits the connectivity between historical states and measurements. Unfortunately, the improvements from the FGO are still limited if the GNSS measurements were not well modeled. The maximum error still reached 23.56 meters. The positioning error still fluctuates dramatically between epochs 190 and 205 (left-hand side of Fig. 11). The main reason for this variability is the high number of unmodeled NLOS measurements. With the use of the proposed method, the 2D mean error decreased from 3.64 meters (FG) to 2.8 (FG-3DLA) meters. The standard deviation was also reduced to 1.62 meters. The maximum 2D error was reduced from 23.56 meters (FG) to 9.71 meters. These improved results show the effectiveness of the proposed method. Although GNSS standalone positioning using the proposed CR-WLS still reaches 7.92 meters, GNSS/INS integration using FGO can effectively make the best use of the pseudorange correction (model calibration in Section 4.2) and uncertainty modeling (model repair in Section 4.3). After applying the 3D LiDAR aided GNSS positioning, the performance of GNSS/INS integration using the state-of-the-art factor graph was pushed significantly higher.

Table 6. Positioning performance of GNSS/INS integration in Urban Canyon 1

GNSS/INS	EKF	FG	FG-3DLA
Mean error	8.03 m	3.64 m	2.80 m
Std. dev.	7.60 m	3.19 m	1.62 m
Maximum error	44.55	23.56 m	9.71m

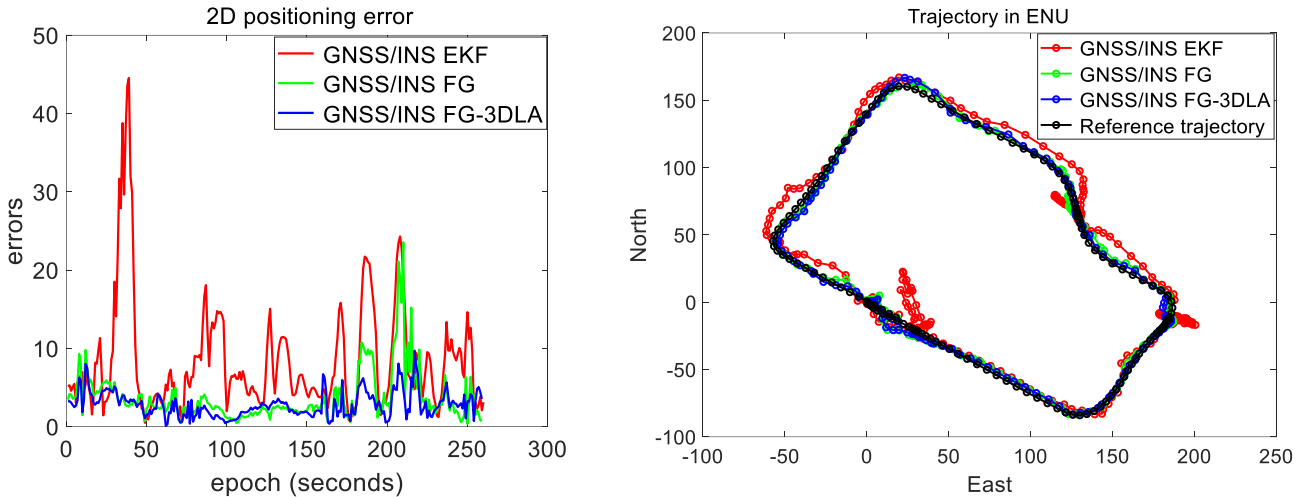


Fig. 11. 2D positioning error and trajectories of the GNSS/INS integrations in Urban Canyon 1

6.3 Evaluation of the Urban Canyon 2 Experiment

To investigate the performance of the proposed method, another experiment was conducted in a denser urban canyon. (Fig. 9). As with Experiment 1, NLOS satellites with high elevation angles cannot be fully detected using the SWM. We also wanted to explore what would happen in a denser urban canyon, using the proposed method.

6.3.1 GNSS Standalone Positioning

As with Experiment 1, the results of the GNSS standalone positioning experiment are presented to show the effectiveness of the proposed method in GNSS positioning. A positioning error of 30.68 meters was obtained using the u-blox receiver with a maximum error of 92.32 meters. A GNSS positioning error of 23.79 meters was obtained using WLS based on the raw pseudorange measurements from the u-blox receiver. The maximum error increased slightly to 104.83 meters, compared with the GNSS positioning using data directly from the u-blox receiver. After excluding all detected NLOS satellites from the GNSS positioning (WLS-NE), both the mean and standard deviation increased to 25.14 and 23.73 meters, respectively. The availability of GNSS positioning data decreased to 95.52%, due to the lack of satellites for GNSS positioning, which again shows that complete NLOS exclusion is not optimal in urban canyons. With the help of NLOS remodeling (Section 4.3), the 2D error decreased to 19.61 meters by R-WLS. One hundred percent availability is guaranteed. The GNSS positioning error was further decreased to 17.09 meters using the CR-WLS method. The improvement in the results shows the effectiveness of the proposed method for GNSS standalone positioning. The maximum error still reached 71.28 meters, because not all NLOS satellites can be detected and mitigated.

To further investigate these results, we also examined the percentage of NLOS satellites within certain elevation angle ranges. The percentage trend is almost opposite the trend in Experiment 1. The majority (44%) of the NLOS satellites belonged to the 60°–90° group in Experiment 2. However, the majority of NLOS satellites belonged to the 0°–30° group in Experiment 1. In Experiment 2 the buildings were higher, and the streets narrower, than in Experiment 1 (Fig. 9). Apart from undetected NLOS satellites, the error caused by multipath effects was not mitigated. Even so, improved GNSS standalone positioning results were obtained, with the 2D error decreasing from 23.79 meters (WLS) to 17.09 (CR-WLS) meters. The NLOS detection accuracy for the satellites in the low elevation angle group (0°–30°) was still more than 90%, similar to Experiment 1. The NLOS detection accuracy for the satellites of the high elevation angle group (60°–90°) was limited (12%). However, the proposed method can easily be adapted to ADV with multiple 3D LiDARs to further detect NLOS satellites with high elevation angles. Since the proposed NLOS detection method relies on the orientation from the AHRS, we also present the effect of orientation error on NLOS detection accuracy. The last row of Table 8 shows the accuracy of NLOS detection at different angle ranges, using the ground truth orientation provided by the SPAN-CPT. Accuracy increased slightly.

Table 7. Positioning performance of GNSS SPP in Urban Canyon 2

GNSS Positioning	u-blox	WLS	WLS-NE	R-WLS	CR-WLS
Mean error	30.68 m	23.79 m	25.14 m	19.61 m	17.09 m
Std. dev.	26.53 m	18.22 m	23.73 m	19.80 m	20.95 m
Maximum error	92.32	104.83 m	109.30	86.14 m	71.28 m
Availability	100%	100%	95.52%	100%	100%

Table 8. Performance of NLOS classification between different elevation ranges in Urban Canyon 2

All data	Elevation (0°–30°)	Elevation (30°–60°)	Elevation (60°–90°)
Percentage of NLOS Satellites	17.7 %	38.3%	44.0 %
Accuracy of NLOS Detection at Different Angle	90.7 %	46.0%	12.0%
Accuracy of NLOS Detection at Different Angle (SPAN-CPT)	91.3 %	47.1%	12.5%

6.3.2 GNSS/INS Integrated Positioning

In this section, we present the results of GNSS/INS integration. Table 9 shows the 2D positioning errors using the three kinds of GNSS/INS integration, similar to Experiment 1. A 2D mean error of 20.89 meters was obtained using EKF, with a maximum error of 90.27 meters. Slightly improved positioning accuracy was obtained after applying the state-of-the-art factor graph, with the mean error decreasing from 20.89 to 18.54 meters. Both the standard deviation and the maximum error decreased. The improvement caused by the state-of-the-art factor graph was not as large as that in Experiment 1, because the percentage of polluted GNSS signals (multipath effects and NLOS receptions) is significantly larger in Urban Canyon 2, which has taller buildings and narrower streets. The improvements from the use of FGO were still limited since the GNSS measurements are not well modeled.

With the use of the proposed method, the 2D mean error decreased from 18.54 meters (FG) to 13.32 (FG-3DLA) meters. The standard deviation was also reduced to 10.11 meters. The maximum 2D error was reduced from 77.10 meters (FG) to 43.82 meters. The improved results show the effectiveness of the proposed method. Fig. 13 shows the positioning errors and trajectories generated in Experiment 2. Positioning was improved almost throughout the experiment. From epoch 350 to epoch 450 the positioning error decreased. Interestingly, the positioning error from FG-3DLA near epoch 300 was even larger than the one from FG which is mainly caused due to the misclassification of satellite visibility. Although the GNSS standalone positioning using the proposed CR-WLS still reached 17.09 meters, the GNSS/INS integration using FGO could make the best use of the pseudorange correction (model calibration in Section 4.2) and uncertainty modeling (model repair in Section 4.3) with the positioning error decreasing to 13.32 meters.

Table 9. Positioning performance of GNSS/INS integration in Urban Canyon 1

GNSS/INS	EKF	FG	FG-3DLA
Mean error	20.89 m	18.54 m	13.32 m
Std. dev	23.44 m	19.18 m	10.11 m
Maximum error	90.27 m	77.10 m	43.82 m

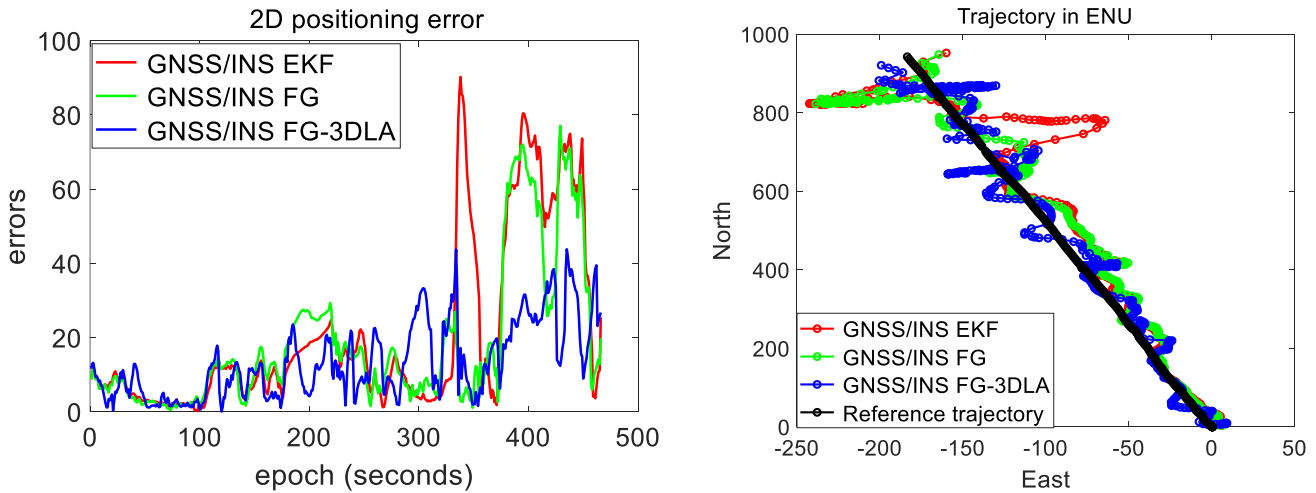


Fig. 13. 2D positioning error and trajectories of the GNSS/INS integrations in Urban Canyon 1

Although the mean positioning error was significantly improved compared with the 30.68 meters obtained using u-blox, it still reached 13.32 meters. The remaining error arises from two major sources: 1) undetected NLOS satellites; and 2) unexpected multipath effects. Table 10 shows the pseudorange errors caused by the multipath effects and NLOS. Satellite 15 introduced the maximum pseudorange error of 37.92 meters among the six satellites. Multipath effects can also cause errors of with similar magnitude; for example, satellite 21 had a pseudorange error of 34.88 meters. Therefore, unmodeled multipath is a major factor causing the remaining 13.32 meters of positioning error. Fortunately, the multipath can be further mitigated using a higher level GNSS antenna, which is acceptable for autonomous driving vehicles.

Table 10. Pseudorange errors in Urban Canyon 2 (Epoch 401793)

Satellite PRN	Elevation Angle (degree)	C/N ₀ (dB-Hz)	Type	Pseudorange Error
15	51.6	31	NLOS	37.29 m
21	48.70	26	Multipath	34.88 m
89	63.1	27	NLOS	5.71 m
92	61.63	33	Multipath	5.49 m
94	62.32	32	Multipath	5.14 m
102	60.98	34	Multipath	7.77 m

7. CONCLUSIONS AND FUTURE WORK

GNSS positioning is currently still the major source of globally referenced positioning for intelligent transportation systems (ITS). However, accurate GNSS positioning in urban canyons is still a challenging problem. NLOS receptions currently remain the major problems for GNSS positioning in urban canyons. Therefore, effectively identifying and mitigating the effects of NLOS receptions is a significant step in achieving and popularizing accurate GNSS positioning solutions, such as SPP, real-time kinematic (RTK) and precise point positioning, in urban canyons. Since the performance of GNSS positioning relies heavily on environmental conditions, the state-of-the-art range-based 3DMA method proposes to effectively mitigate NLOS effects, based on offline environment descriptions known as 3D building models. However, with the increasing complexity and dynamics of city infrastructures, 3D building models cannot fully describe the real-time environment. Reconstructing the real-time environment based on onboard sensing is a promising method for identifying potentially polluted GNSS signals. Unlike the state-of-the-art 3DMA GNSS method, this paper proposes a novel 3D LiDAR aided GNSS positioning method which makes use of an onboard 3D LiDAR sensor to reconstruct the surrounding environment. Potential NLOS receptions caused by static buildings, dynamic objects and even semi-static infrastructure (traffic signpost in Fig. 10) can be detected, remodeled and even corrected. This paper reports a continuation of the previous work described in [5] [9] [38]. Three drawbacks listed in Section 1 are alleviated, and a general solution is proposed to mitigate the effects of NLOS receptions. The method proposed in this paper can be easily adapted to the systems with multiple 3D LiDARs, and NLOS satellites with high elevation angles can be detected accordingly. Overall, we believe that the proposed method can have a positive impact on both the academic and industrial fields.

Since the remaining positioning error still reaches about 10 meters in the dense Urban Canyon 2, we will integrate the LiDAR odometry with the proposed method in future work. The accuracy of the orientation could also be enhanced with the use of LiDAR odometry to further improve the performance of NLOS detection.

REFERENCES

1. Geiger, A., P. Lenz, and R. Urtasun. *Are we ready for autonomous driving? the kitti vision benchmark suite*. in *2012 IEEE Conference on Computer Vision and Pattern Recognition*. 2012. IEEE.
2. Rödel, C., et al. *Towards autonomous cars: the effect of autonomy levels on acceptance and user experience*. in *Proceedings of the 6th International Conference on Automotive User Interfaces and Interactive Vehicular Applications*. 2014. ACM.
3. Groves, P.D., *Principles of GNSS, inertial, and multisensor integrated navigation systems*. 2013: Artech house.
4. Hsu, L.-T., *Analysis and modeling GPS NLOS effect in highly urbanized area*. *GPS solutions*, 2018. **22**(1): p. 7.
5. Wen, W., G. Zhang, and L.-T. Hsu. *Exclusion of GNSS NLOS receptions caused by dynamic objects in heavy traffic urban scenarios using real-time 3D point cloud: An approach without 3D maps*. in *Position, Location and Navigation Symposium (PLANS), 2018 IEEE/ION*. 2018. IEEE.
6. Breßler, J., et al. *GNSS positioning in non-line-of-sight context—A survey*. in *Intelligent Transportation Systems (ITSC), 2016 IEEE 19th International Conference on*. 2016. IEEE.
7. Pinana-Diaz, C., et al. *GPS multipath detection and exclusion with elevation-enhanced maps*. in *Intelligent transportation systems (ITSC), 2011 14th International IEEE Conference on*. 2011. IEEE.
8. Peyraud, S., et al., *About non-line-of-sight satellite detection and exclusion in a 3D map-aided localization algorithm*. *Sensors*, 2013. **13**(1): p. 829-847.
9. Weisong Wen, G.Z., Li-ta Hsu, *Correcting GNSS NLOS by 3D LiDAR and Building Height*, in *ION GNSS+, 2018*. 2018: Miami, Florida, USA.
10. Wang, L., P.D. Groves, and M.K. Ziebart. *Urban positioning on a smartphone: Real-time shadow matching using GNSS and 3D city models*. 2013. The Institute of Navigation.
11. Wang, L., P.D. Groves, and M.K. Ziebart, *GNSS shadow matching: Improving urban positioning accuracy using a 3D city model with optimized visibility scoring scheme*. *Navigation*, 2013. **60**(3): p. 195-207.
12. Wang, L., P.D. Groves, and M.K. Ziebart, *Smartphone shadow matching for better cross-street GNSS positioning in urban environments*. *The Journal of Navigation*, 2015. **68**(3): p. 411-433.
13. Groves, P.D. and M. Adjrjad, *Likelihood-based GNSS positioning using LOS/NLOS predictions from 3D mapping and pseudoranges*. *GPS Solutions*, 2017. **21**(4): p. 1805-1816.
14. Adjrjad, M. and P.D. Groves, *Intelligent Urban Positioning: Integration of Shadow Matching with 3D-Mapping-Aided GNSS Ranging*. *Journal of Navigation*, 2018. **71**(1): p. 1-20.
15. Hsu, L.-T., Y. Gu, and S. Kamijo, *3D building model-based pedestrian positioning method using GPS/GLONASS/QZSS and its reliability calculation*. *GPS Solutions*, 2016. **20**(3): p. 413-428.
16. Miura, S., et al., *GPS error correction with pseudorange evaluation using three-dimensional maps*. *IEEE Transactions on Intelligent Transportation Systems*, 2015. **16**(6): p. 3104-3115.
17. Obst, M., et al. *Multipath detection with 3D digital maps for robust multi-constellation GNSS/INS vehicle localization in urban areas*. in *Intelligent Vehicles Symposium (IV), 2012 IEEE*. 2012. IEEE.
18. Suzuki, T. and N. Kubo, *Correcting GNSS multipath errors using a 3D surface model and particle filter*. *Proc. ION GNSS+ 2013*, 2013.
19. Ng, H.-F., Zhang, G., Hsu, Li-Ta, *GNSS NLOS Pseudorange Correction based on Skymask for Smartphone Applications*, in *ION GNSS+, 2019*. 2019: Miami, Florida, USA.
20. Pfeifer, T. and P. Protzel. *Expectation-maximization for adaptive mixture models in graph optimization*. in *2019 International Conference on Robotics and Automation (ICRA)*. 2019. IEEE.
21. Pfeifer, T. and P. Protzel. *Robust sensor fusion with self-tuning mixture models*. in *2018 IEEE/RSJ International Conference on Intelligent Robots and Systems (IROS)*. 2018. IEEE.
22. Pfeifer, T., S. Lange, and P. Protzel. *Dynamic Covariance Estimation—A parameter free approach to robust Sensor Fusion*. in *2017 IEEE International Conference on Multisensor Fusion and Integration for Intelligent Systems (MFI)*. 2017. IEEE.
23. Sünderhauf, N. and P. Protzel. *Towards robust graphical models for GNSS-based localization in urban environments*. in *International Multi-Conference on Systems, Signals & Devices*. 2012. IEEE.
24. Dellaert, F. and M. Kaess, *Factor graphs for robot perception*. *Foundations and Trends® in Robotics*, 2017. **6**(1-2): p. 1-139.

25. Sünderhauf, N., et al. *Switchable constraints and incremental smoothing for online mitigation of non-line-of-sight and multipath effects*. in *2013 IEEE Intelligent Vehicles Symposium (IV)*. 2013. IEEE.
26. Barfoot, T.D., *State Estimation for Robotics*. 2017: Cambridge University Press.
27. Watson, R.M. and J.N. Gross, *Robust navigation in GNSS degraded environment using graph optimization*. arXiv preprint arXiv:1806.08899, 2018.
28. Watson, R.M., et al., *Uncertainty Model Estimation in an Augmented Data Space for Robust State Estimation*. arXiv preprint arXiv:1908.04372, 2019.
29. Watson, R.M., et al., *Robust Incremental State Estimation through Covariance Adaptation*. arXiv preprint arXiv:1910.05382, 2019.
30. Sánchez, J.S., et al. *Use of a FishEye camera for GNSS NLOS exclusion and characterization in urban environments*. in *ION ITM 2016, International Technical Meeting*. 2016. ION.
31. Kato, S., et al., *Nlos satellite detection using a fish-eye camera for improving gnss positioning accuracy in urban area*. *Journal of robotics and mechatronics*, 2016. **28**(1): p. 31-39.
32. Meguro, J.I., et al., *GPS multipath mitigation for urban area using omnidirectional infrared camera*. *IEEE Transactions on Intelligent Transportation Systems*, 2009. **10**(1): p. 22-30.
33. Suzuki, T., et al. *High-accuracy GPS and GLONASS positioning by multipath mitigation using omnidirectional infrared camera*. in *IEEE International Conference on Robotics and Automation*. 2011.
34. Gakne, P.V., *Improving the Accuracy of GNSS Receivers in Urban Canyons using an Upward-Facing Camera*. 2018, PhD Thesis, Geomatics Engineering, University of Calgary. doi: dx. doi. org ...
35. Gakne, P.V. and K. O'Keefe, *Tightly-Coupled GNSS/Vision Using a Sky-Pointing Camera for Vehicle Navigation in Urban Areas*. *Sensors*, 2018. **18**(4): p. 1244.
36. Mur-Artal, R., J.M.M. Montiel, and J.D. Tardos, *ORB-SLAM: a versatile and accurate monocular SLAM system*. *IEEE Transactions on Robotics*, 2015. **31**(5): p. 1147-1163.
37. Wen W., B.X., Kan Y.C., Hsu, L.T, *Tightly Coupled GNSS/INS Integration Via Factor Graph and Aided by Fish-eye Camera (Accepted)*. *IEEE Transactions on Vehicular Technology*, 2019.
38. X., W., W., Zhang, G., Hsu, Li-Ta, *Real-time GNSS NLOS Detection and Correction Aided by Sky-Pointing Camera and 3D LiDAR*, in *Proceedings of ION Pacific PNT 2019*. 2019: Honolulu, HA, USA.
39. Weisong Wen, Y.C.K., Li-Ta Hsu, *Performance Comparison of GNSS/INS Integrations Based on EKF and Factor Graph Optimization*, in *ION GNSS+ 2019*. 2019: Florida.
40. Moosmann, F. and C. Stiller. *Velodyne slam*. in *2011 IEEE intelligent vehicles symposium (iv)*. 2011. IEEE.
41. Hsu, L.-T., Y. Gu, and S. Kamijo, *NLOS correction/exclusion for GNSS measurement using RAIM and city building models*. *Sensors*, 2015. **15**(7): p. 17329-17349.
42. Bailey, T. and H. Durrant-Whyte, *Simultaneous localization and mapping (SLAM): Part II*. *IEEE robotics & automation magazine*, 2006. **13**(3): p. 108-117.
43. Zhang, J. and S. Singh. *LOAM: Lidar Odometry and Mapping in Real-time*. in *Robotics: Science and Systems*. 2014.
44. Geiger, A., et al., *Vision meets robotics: The KITTI dataset*. *The International Journal of Robotics Research*, 2013. **32**(11): p. 1231-1237.
45. Kaplan, E. and C. Hegarty, *Understanding GPS: principles and applications*. 2005: Artech house.
46. Jurado, J.D. and J.F. Raquet. *Towards an online sensor model validation and estimation framework*. in *2018 IEEE/ION Position, Location and Navigation Symposium (PLANS)*. 2018. IEEE.
47. Wen, W., L.-T. Hsu, and G.J.S. Zhang, *Performance analysis of NDT-based graph SLAM for autonomous vehicle in diverse typical driving scenarios of Hong Kong*. 2018. **18**(11): p. 3928.
48. Greenspan, M. and M. Yurick. *Approximate kd tree search for efficient ICP*. in *Fourth International Conference on 3-D Digital Imaging and Modeling, 2003. 3DIM 2003. Proceedings.* 2003. IEEE.
49. Glassner, A.S., *An introduction to ray tracing*. 1989: Elsevier.
50. Tay, S. and J. Marais. *Weighting models for GPS Pseudorange observations for land transportation in urban canyons*. in *6th European Workshop on GNSS Signals and Signal Processing*. 2013.
51. Herrera, A.M., et al., *goGPS: open-source MATLAB software*. *GPS solutions*, 2016. **20**(3): p. 595-603.
52. Indelman, V., et al. *Factor graph based incremental smoothing in inertial navigation systems*. in *2012 15th International Conference on Information Fusion*. 2012. IEEE.
53. Kaess, M., et al., *iSAM2: Incremental smoothing and mapping using the Bayes tree*. *The International Journal of Robotics Research*, 2012. **31**(2): p. 216-235.
54. Sünderhauf, N., et al. *Multipath mitigation in GNSS-based localization using robust optimization*. in *2012 IEEE Intelligent Vehicles Symposium*. 2012. IEEE.
55. Dellaert, F., *Factor graphs and GTSAM: A hands-on introduction*. 2012, Georgia Institute of Technology.
56. Quigley, M., et al. *ROS: an open-source Robot Operating System*. in *ICRA workshop on open source software*. 2009. Kobe, Japan.

57. Falco, G., M. Pini, and G. Marucco, *Loose and tight GNSS/INS integrations: Comparison of performance assessed in real urban scenarios*. *Sensors*, 2017. **17**(2): p. 255.
58. Jiao, J., et al., *Automatic Calibration of Multiple 3D LiDARs in Urban Environments*. arXiv preprint arXiv:1905.04912, 2019.
59. Silva, C.M., et al., *A survey on infrastructure-based vehicular networks*. *Mobile Information Systems*, 2017. **2017**.